CARLOS III UNIVERSITY OF MADRID

POLYTECHNIC

DEGREE: **INDUSTRIAL ENGINEER**

Proyecto Fin de Carrera

MATERIALS DEPARTMENT

# Formability of an ultra-fine grained Cu-Cr-Zr alloy processed via severe plastic deformation


PEDRO ASENJO VARELA JULY 2015

Título: “Formability of an ultra-fine grained Cu-Cr-Zr alloy processed via severe plastic deformation”

Autor: PEDRO ASENJO VARELA

Director: ILCHAT SABIROV

EL TRIBUNAL

Presidente: Antonia Jiménez Morales.

Vocal: Emilio Olías Ruiz.

Secretario: Alicia Paez Pavón.

Realizado el acto de defensa y lectura del Proyecto Fin de Carrera el día _16_ de JULIO de 2015 en Leganés, en la Escuela Politécnica Superior de la Universidad Carlos III de Madrid, acuerda otorgarle la CALIFICACIÓN de

VOCAL

SECRETARIO PRESIDENTE

I approved the presentation of this project

Formability of an ultra-fine grained Cu-Cr-Zr alloy processed via severe plastic deformation

Executed by

PEDRO ASENJO VARELA

Guided by

Dr. JOSE MANUEL TORRALBA

and

Dr. ILCHAT SABIROV

IMDEA Materials Institute

Signed: Prof. JOSE MANUEL TORRALBA

*Date:* .....

**Acknowledgements**

First of all, I want to thank IMDEA Materials Institute for the opportunity that they have given to me from the first moment in order to have access to all the information and facilities needed. Without them I could not have carried out this project.

Also I would like to thank the Polytechnic Carlos III University for all these formation years and its implication and support in the development of this Final Degree Project.

I have to acknowledge the effort that two persons have made. Without their support both inside and outside IMDEA I would not have achieved my goal. Ilchat Sabirov, Researcher at IMDEA Materials Institute I work with and Jose Manuel Torralba Deputy Director of IMDEA Materials Institute and my project coordinator at the university. I would like to acknowledge gratefully thank Marcos Angulo for all the technical support in the laboratory every time I needed it.

Without any doubt without their collaboration I would not have been able to develop my project in such a satisfactory way.

## Agradecimientos

Este Proyecto, que significa la obtención del título de Ingeniería Industrial Superior, va dedicado a todos aquellos que me han ayudado y motivado para conseguirlo.

Mención especial a mi abuelo, Higinio Varela Sánchez, Doctor Ingeniero Industrial que se que me estará viendo desde el cielo y a mi madre Paloma Varela García de Oteyza, Ingeniera Industrial, va dedicada la parte de motivación. Desde pequeño quería ser como ellos. Mi padre y mi hermano, que siempre me han ayudado y aguantado y todos mis tíos, primos y demás abuelos que siempre han estado ahí preocupándose y alegrándose de mis logros.

Mis amigos y compañeros de carrera que han sufrido conmigo y con los que tanto tiempo he pasado y seguiré pasando. María, Pablo y David con los que compartí la maravillosa experiencia del Erasmus y Kiko, Chema, Alberto Casado, Alberto Álvarez y Víctor con los que tantos trabajos y asignaturas he compartido.

Dedicado a todos vosotros y al Señor que tantas fuerzas me ha dado.

# ABSTRACT

Ultra-fine grained (UFG) metallic materials have been a hot topic in materials science for more than 25 years. There is a significant body of research showing that the UFG materials have very high mechanical strength, but their commercialization is limited due to their low uni-axial tensile ductility. The main objective of this thesis is to study the bi-axial stretching formability of the UFG Cu-Cr-Zr alloy material after equal channel angular pressing with two different processing routes. It is demonstrated that there is effect of the microstructure and stress state (stress tri-axiality) on the strain rate sensitivity of the UFG Cu-Cr-Zr alloy. The UFG alloy shows higher strain rate sensitivity in the uni-axial tensile mode compared to the biaxial stretching mode. The microstructure of the UFG Cu-Cr-Zr alloy depends on the processing route and can be designed in such a way, so it shows very high biaxial stretching formability, comparable to that of its coarse-grained counterpart, sufficient for metalforming operations. The effect of microstructure on strength, uni-axial tensile ductility and biaxial stretching formability is discussed.

# RESUMEN

Los materiales metálicos de grano ultra fino han sido un tema candente en la ciencia de materiales durante más de 25 años. Existe una gran investigación que demuestra la muy alta resistencia mecánica de los materiales de grano ultra fino, pero debido a su baja ductilidad a tracción uni-axial, su comercialización es limitada. El objetivo principal de esta tesis es el estudio de la formabilidad por estiramiento biaxial de la microestructura de una aleación de Cu-Cr-Zr de grano ultra fino, después de aplicarle presión en canal angular constante con dos tipos de procesado diferentes. Está demostrado que existe efecto de la microestructura y del estado tensional (tensión tri-axial) en la sensibilidad de la velocidad de deformación de la aleación de Cu-Cr-Zr de grano ultra fino. La aleación de grano ultra fino muestra mayor sensibilidad a la velocidad de deformación en el modo tensional uni-axial que en el modo de estiramiento biaxial. La microestructura de la aleación de Cu-Cr-Zr de grano ultra fino depende del procesado realizado y puede ser diseñado de tal manera, que muestre una muy alta formabilidad por estiramiento biaxial, comparada con la del grano grueso, suficiente para el conformado de metales. A continuación se discute el efecto de la microestructura en resistencia, ductilidad a tracción uni-axial y formabilidad por estiramiento biaxial.

# Table of Contents

# Table of Figures

# Table index

# 1 INTRODUCTION

# 1. Introduction

This work focuses on biaxial stretching formability of ultra-fine grained Cu-Cr-Zr alloy processed via severe plastic deformation using two different processing routes, which resulted in different microstructures. The effect of processing routes on the microstructure, tensile mechanical properties, biaxial stretching formability, and strain rate sensitivity is carefully studied. It is demonstrated that ultra-fine grained Cu-Cr-Zr alloy can show formability sufficient for metal forming operations, even if its uni-axial tensile ductility is low.

## 1.1. Ultra-fine grained metallic materials

Ultra-fine grained (UFG) metallic materials have been a hot topic in materials science over last 25 years. [1].

In 1988, the first report was published demonstrating the potential for achieving ultrafine grains within the submicrometer range through the application of severe plastic deformation (SPD) to conventional bulk coarse-grained metallic materials resulting in significant enhancement of their properties [2]. Nowadays, this approach is generally termed SPD processing. After this publication, the SPD processed materials with submicrocrystalline structure attracted a lot of attention that led to the initiation and development of many research activities around the world devoted to processing and measuring their characteristics. It is interesting to note that the research activity in this field has both continued to develop and very much expanded up to the present date [3].

The SPD concept is based on the fact that a metal specimen subjected to high plastic strains, $\varepsilon >$ 4-6 with complex stress state under very high hydrostatic pressure, leading to refining the coarse grains down into submicro- and nanograins. Thus, the SPD has often been referred to as 'top-down' approach. Depending on the final grain size, the materials with ultrafine grained (UFG) structure have been classified as:
1*) Ultra-fine grained materials* are materials with a grain size in the range of 100 - 1000 nm;
2) *Nanocrystalline materials* are materials with a grain size below 100 nm.

The main SPD processing techniques developed up to date for fabrication of UFG metallic materials are considered in details in the next Section.

## 1.2. Main processing methods of severe plastic deformation

### 1.2.1. Equal-Channel Angular Pressing (ECAP)

#### 1.2.1.1. Conventional ECAP with rods and bars

There are a number of reports describing the fundamental process of metal flow during ECAP [4 - 9] and the principle of ECAP is illustrated schematically in Fig. 1. For the die shown in the illustration, the internal channel is bent through an abrupt angle, Φ, equal to 90º and there is an additional angle, Ψ, equal to 0º in Fig. 1, which represents the outer arc of curvature where the two channels intersect. The sample, in the form of a rod or bar, is machined to fit within the channel and the die is placed in some form of press so that the sample can be pressed through the die using a plunger. The nature of the imposed deformation is simple shear which occurs as the sample passes through the die as shown schematically in Fig. 2: for simplicity, the die angle in Fig. 2 is 90º, the theoretical shear plane is shown between two adjacent elements within the sample numbered 1 and 2, and these elements are transposed by shear as depicted in the lower part of the diagram. Despite the introduction of a very intense strain as the sample passes through the shear plane, the sample ultimately emerges from the die without experiencing any change in the cross-sectional dimensions. This is illustrated by the pressed sample in Fig. 1. Three separate orthogonal planes are also defined in Fig. 1 where these planes are the X or transverse plane perpendicular to the flow direction, the Y or flow plane parallel to the side face at the point of exit from the die and the Z or longitudinal plane parallel to the top surface at the point of exit from the die, respectively. The retention of the same cross-sectional area when processing by ECAP, despite the introduction of very large strains, is the important characteristic of SPD processing and it is a characteristic which distinguishes this type of processing from conventional metal-working operations such as rolling, extrusion and drawing.

Since the cross-sectional area remains unchanged, the same sample may be pressed repetitively to attain exceptionally high strains. For example, the use of repetitive pressings provides an opportunity to invoke different slip systems on each consecutive pass by simply rotating the samples in different ways between the various passes. In practice, many of the investigations of ECAP involve the use of bars with square cross-sections and dies having square channels. For these samples, it is convenient to develop processing routes in which the billets are rotated by increments of 90º between each separate pass.

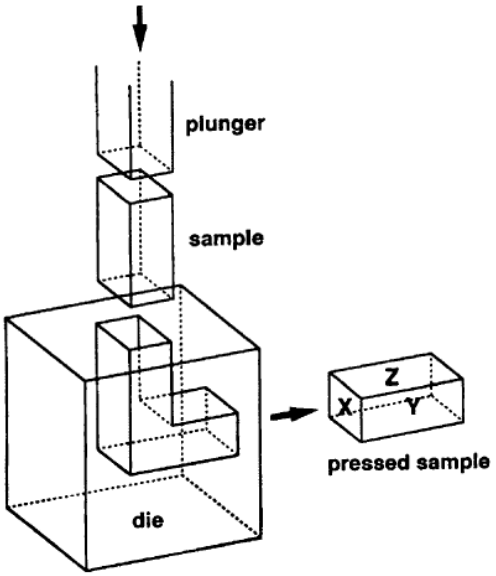


*Fig. 1. Schematic illustration of a typical ECAP facility: the X, Y and Z planes denote the transverse plane, the flow plane and the longitudinal plane, respectively.*

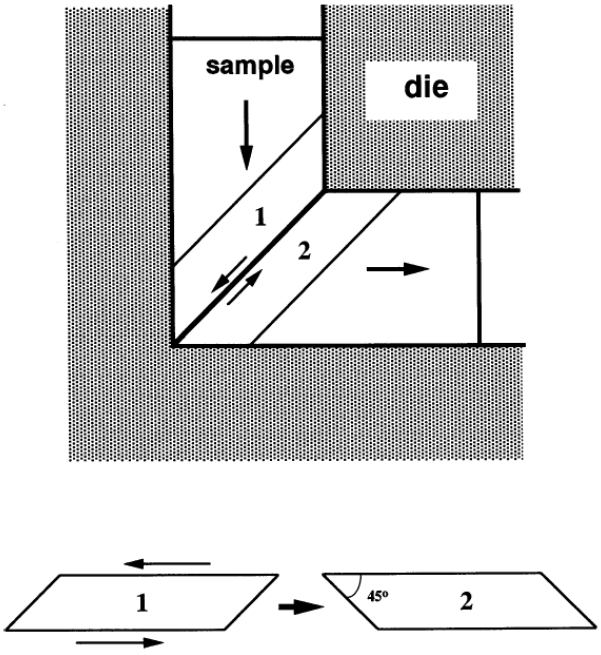


*Fig. 2. The principle of ECAP showing the shearing plane within the die: the elements numbered 1 and 2 are transposed by shear as indicated in the lower part of the illustration.*

The same processing routes are also easily applied when the samples are in the form of rods with circular cross-sections. The fundamental processing routes identified in ECAP will be discussed in detail in the Section 1.2.1.3 below.

### 1.2.1.2. The strain imposed in ECAP

An abrupt strain is imposed on a sample in every passage through an ECAP die. The magnitude of this strain may be estimated using an analytical approach based on the various die configurations illustrated schematically in the two-dimensional representation shown in Fig. 3, where Φ is the channel angle and the angle Ψ represents the angle associated with the arc of curvature where the two parts of the channel intersect. Three conditions are shown in Fig. 3: thus, Fig. 3(a) corresponds to a limiting situation where $\Psi = 0^o$, Fig. 3(b) corresponds to a second limiting situation where $\Psi = (\pi - \Phi)$ and Fig. 3(c) represents an intermediate condition where $0^o < \Psi < (\pi - \Phi)^o$. The strain is estimated by assuming a fully-lubricated specimen so that any frictional effects may be neglected.

For the situation where $\Psi = 0^o$ in Fig. 3(a), a small square element in the entrance channel, labelled **abcd**, passes through the theoretical shear plane and becomes distorted into the parallelogram labelled **a'b'c'd'**. It can be shown from first principles that the shear strain, γ, is given by

$$\gamma = 2 \cot\left(\frac{\Phi}{2}\right) \qquad (1)$$

Using the same approach for Fig. 3(b), it follows that

$$\gamma = \Psi \qquad (2)$$

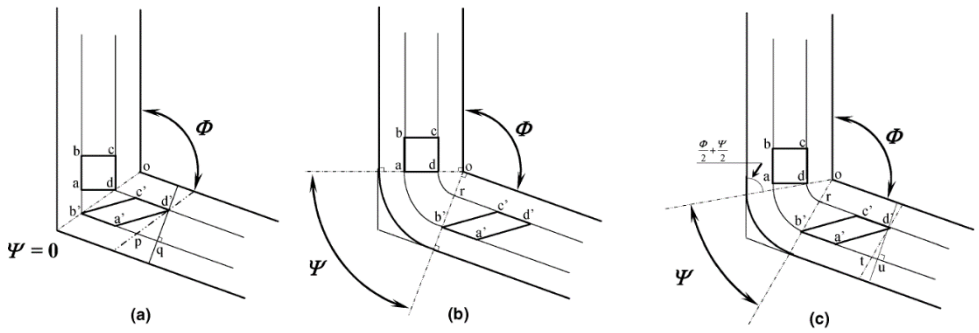


*Fig. 3. Principle of ECAP where Φ is the angle of intersection of the two channels and Ψ is the angle subtended by the arc of curvature at the point of intersection: (a) Ψ = 0, (b) Ψ = π - Φ, (c) an arbitrary value of Ψ lying between Ψ = 0 and Ψ = π - Φ.*

and a similar analysis for Fig. 3(c) leads to the general solution

$$\gamma = 2\cot\left(\frac{\Phi}{2}+\frac{\psi}{2}\right) + \Psi cosec\left(\frac{\Phi}{2}+\frac{\psi}{2}\right) \qquad (3)$$

It follows from inspection that the general solution in Eq. (3) reduces to Eq. (1) when $\Psi = 0^o$ and to Eq. (2) when $\Psi = (\pi - \Phi)$. Finally, the equivalent strain after N passes, $\varepsilon_N$, may be expressed in a general form by the relationship [10]

$$\varepsilon_N = \frac{N}{\sqrt{3}}\left[2\cot\left(\frac{\Phi}{2}+\frac{\psi}{2}\right) + \Psi cosec\left(\frac{\Phi}{2}+\frac{\psi}{2}\right)\right] \qquad (4)$$

Eq. (4) is consistent with an earlier estimate of the strain where a die was analyzed with $\Psi = 0^o$, the channel angle $\Phi$ was taken as $2\varphi$ and the strain after N passes was estimated as [4]

$$\varepsilon_N = \frac{N}{\sqrt{3}}\cot g\varphi \qquad (5)$$

Eq. (5) is also identical to the relationship derived in an alternative analysis [11]. Thus, all of these approaches lead to similar relationships for the equivalent strain but Eq. (4) has the advantage that it incorporates the angle associated with the arc of curvature, $\Psi$. Eq. (4) is also reasonably consistent with alternative approaches [12 - 14] and it provides a simple and direct procedure for estimating the strain for any selected die having different values for $\Phi$ and $\Psi$.

There is experimental evidence supporting the use of Eq. (4) in experiments on ECAP. First, model experiments were conducted where layers of colored plasticize were pressed through a Plexiglas die and measurements of the strain in these experiments revealed excellent agreement with Eq. (4) in the central regions of the billets although there were deviations near the cell walls because of frictional effects [15]. Second, model experiments were conducted in which two half-billets of pure aluminium, with a regular rectangular grid drawn on one of their common interfaces, were pressed through a die having $\Phi = 90^o$ and $\Psi = 0^o$ and the strain was measured directly after pressing [16]. The result showed excellent agreement with Eq. (4) throughout 85% of the billet although there was an area of non-uniform deformation occurring in the vicinity of the lower surface of the billet where the material passed through the outer corner of the die. The experiment showed this region of non-uniformity occupied only 15% of the total area.

It is convenient to prepare a graphical representation of Eq. (4) because this provides a simple visual understanding of the significance of the die angles $\Psi$ and $\Phi$. This type of plot was initially constructed for die angles at and above $\Phi = 90^o$ [17] but subsequently the approach was extended to include die angles as small as $45^o$ [18]: the latter approach is

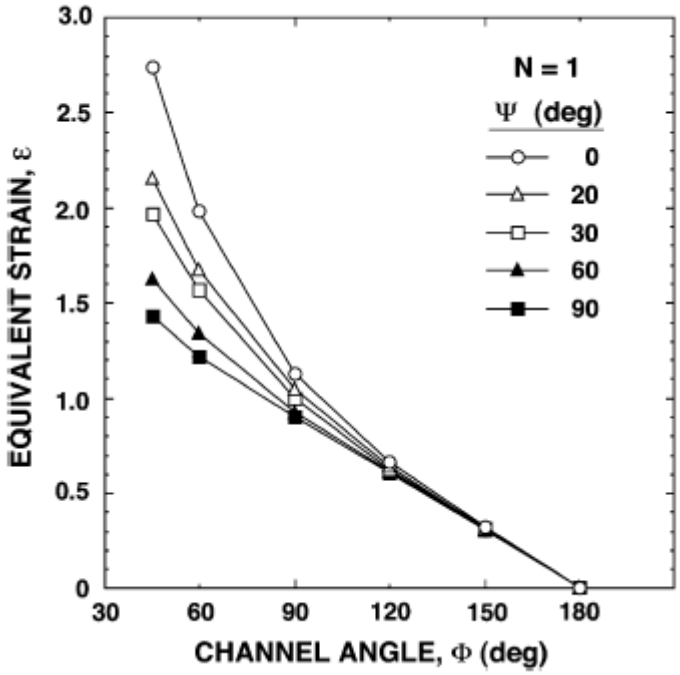


*Fig. 4. Variation of the equivalent strain, ε, with the channel angle, Φ, over an angular range of Φ from 45º to 180º for values of the angle of the arc of curvature, Ψ, from 0º to 90º: the strains are shown for a single pass where N = 1.*

shown in Fig. 4 for a single pass with N = 1 where the channel angle Φ ranges from 45º to 180º and the arc of curvature varies from 0º to 90º.

Several conclusions may be reached from inspection of Fig. 4. First, the angle at the arc of curvature, Ψ, has a relatively minor effect on the equivalent strain except only for channel angles less than 90º. Second, exceptionally high strains may be achieved in a single pass by constructing a die with very low values of Φ and Ψ. Third, for conventional dies where the channel angle is generally equal to 90º, the equivalent strain is close to ≈1 for a single pass and this strain is essentially independent of the angle representing the arc of curvature, Ψ.

### 1.2.1.3. The processing routes in ECAP

There are four basic processing routes in ECAP and these routes introduce different slip systems during the pressing operation so that they lead to significant differences in the microstructures produced by ECAP [19 - 21]. The four different processing routes are summarized schematically in Fig. 5 [22]: thus, in route A the sample is pressed without rotation, in route $B_A$ the sample is rotated by 90º in alternate directions between consecutive passes, in route $B_C$ the sample is rotated by 90º in the same sense (either clockwise or counter-clockwise) between each pass and in route C the sample is rotated by 180º between passes. Various combinations of these routes are also possible, such as combining routes $B_C$ and C by alternating rotations through 90º and 180º after every pass,

but in practice the experimental evidence obtained to date suggests that these more complex combinations lead to no additional improvement in the mechanical properties of the as-pressed materials [23]. Accordingly, for the simple processing of bars or rods, attention is generally devoted exclusively to the four processing routes delineated in Fig. 5.

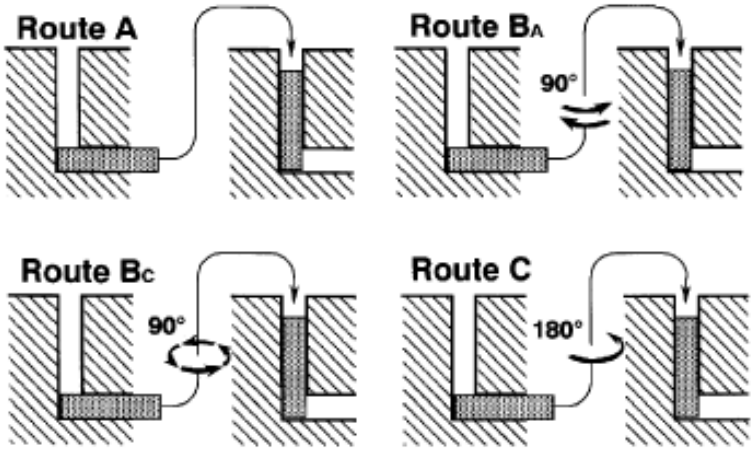


*Fig. 5. The four fundamental processing routes in ECAP processing [22].*

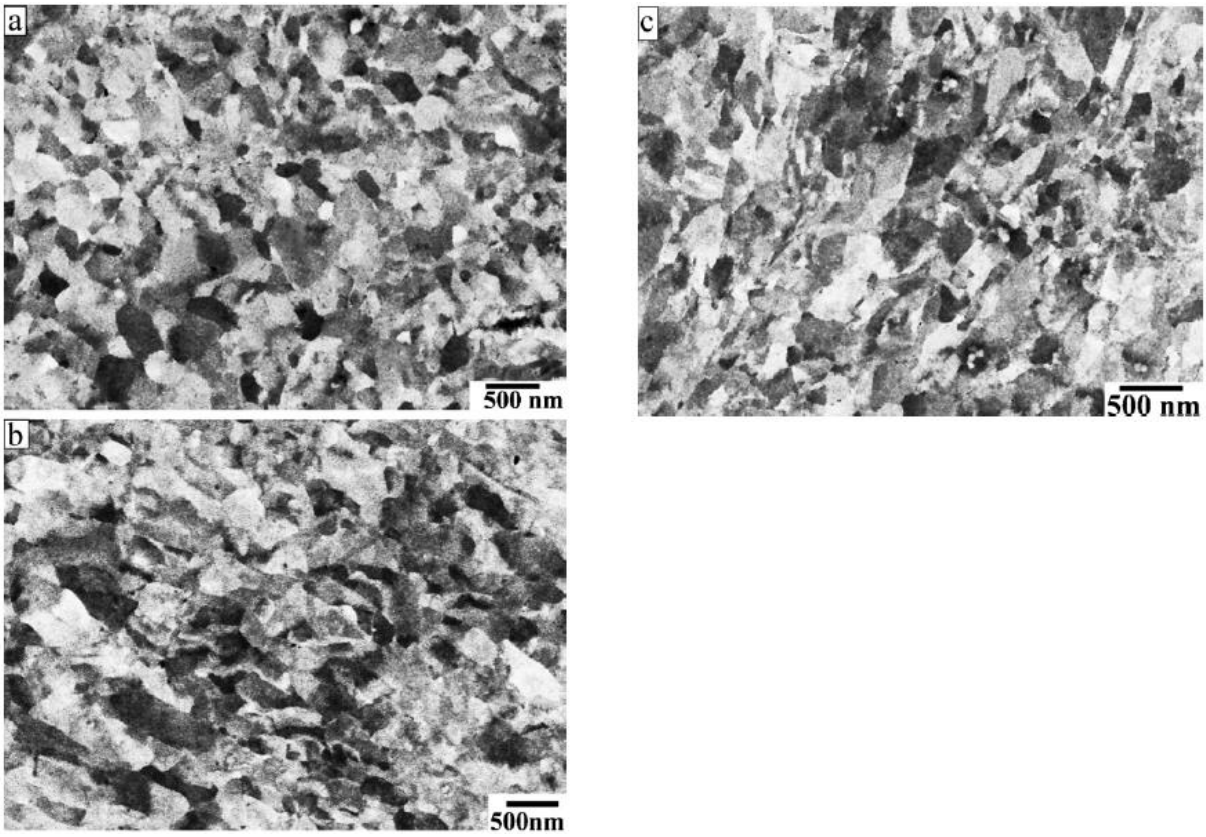


*Fig. 6. SEM images in BSE contrast mode illustrating typical substructures found after ECAP processing of solution treated Cu-Cr-Zr alloy to: (a) 4 ECAP passes, (b) 12 ECAP passes, and (c) 4 ECAP passes and annealed for 1 h at 450 °C [24].*

### 1.2.2. High Pressure Torsion (HPT)

**High pressure torsion (HPT)**. In HPT, a small disk is placed between two anvils and one of them is able to rotate under pressure of several GPa, thus, deforming the disk by pure shear. Schematic illustration of the HPT processing is presented in Figure 6. Although the fundamental principles of this procedure were first proposed more than 70 years ago, processing by HPT became of major importance only within the last 20 years when it was recognized that this metal forming process provides an opportunity for achieving grain refinement. The main advantage of HPT is that under high pressure, very high strains can be induced into sample without its failure, so other mechanisms of microstructure evolution can be evolved once high strains are reached and microstructures with smaller grain sizes can be generated. Even hard to deform metallic materials, such as Tungsten, can be subjected to HPT processing due to very high pressures applied. Two main shortcomings of standard HPT are a small sample size and inhomogeneous strain induced into processed discs leading to inhomogeneous microstructure along the disc radius. The latter can be solved via increase of deformation strain (number of HPT turns) leading to a more homogeneous microstructure along the disc radius though a small unprocessed area might remain in the centre of disc.

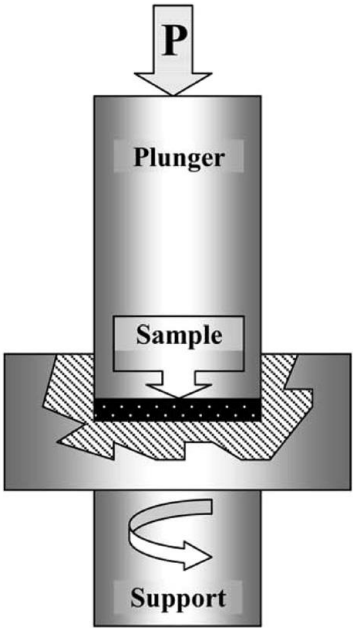


*Fig. 7. Schematic illustration of HPT processing.*

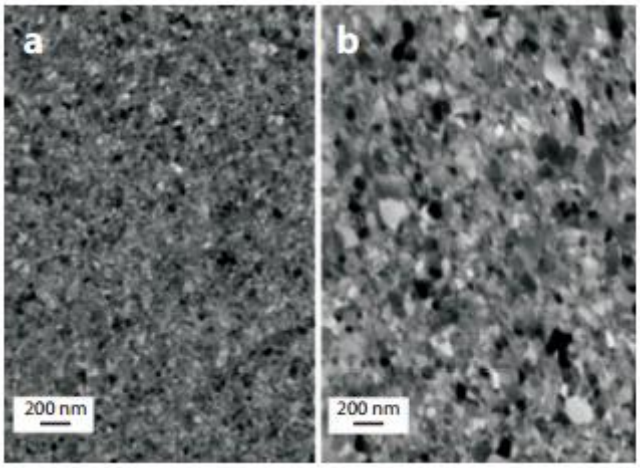


*Fig. 8. Scanning electron micrograph of (a) electrodeposited nanocrystalline Ni and (b) HPT-deformed, electrodeposited Ni in the axial direction. The coarsening of the nanocrystalline Ni due to HPT is obvious [25].*

### 1.2.3. Accumulative Roll Bonding (ARB)

Fig. 9 presents the scheme of accumulative roll bonding (ARB) procedure. Two pieces of strip with clean and degreased surfaces are put together and after annealing joined by means of 50% consecutive rolling. The obtained strip which is composed of two bond layers is then sectioned in two pieces and after cleaning of two surfaces which are fixed together, consecutively heated and rolled 50% to perform roll bonding. Due to 50% rolling reduction followed by stacking two halves and consecutive 50% rolling reduction the procedure can be continued practically without limits.

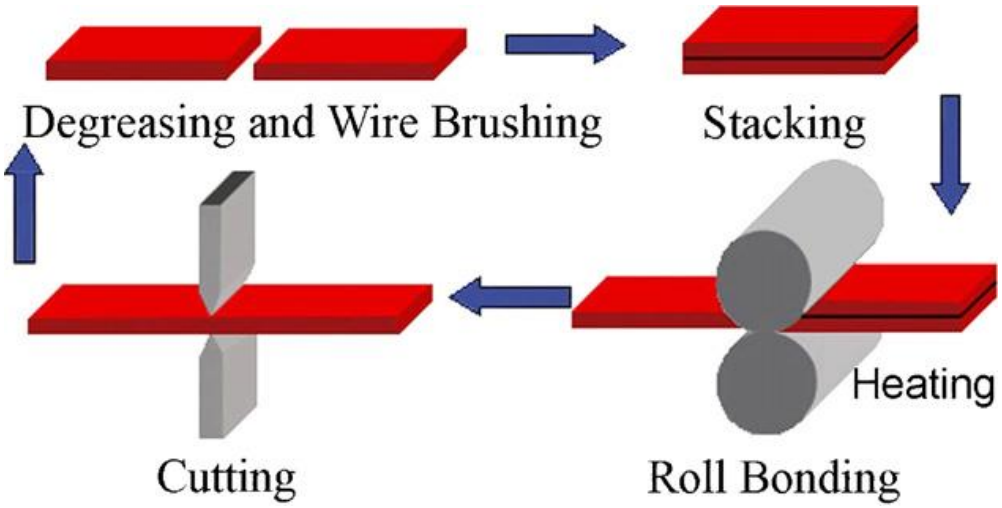


*Fig. 9. Scheme of the accumulative roll-bonding (ARB) process.*

Suppose the strip with initial thickness $t_0$, rolled with 50% reduction each cycle; the thickness $t_n$ of individual layer, after $n$ cycles, can be calculated according to the formula:

$$t_n = t_0/2^n \qquad (6)$$

The total reduction $Z_n$ after $n$ cycles is:

$$Z_n = 1\text{-}t/t_0 = 1\text{-}1/2^n \qquad (7)$$

And with the Huber-Henry-v. Mises yield criterion of plasticity and plane strain of deformation under rolling the equivalent plastic strain $\varepsilon$ is equal to

$$\varepsilon_n = \{\frac{2}{\sqrt{3}} ln\left(\frac{1}{2}\right)\}*n = 0.8n \qquad (8)$$

Assuming initial thickness $t_0$ = 1 mm and performing exemplary $n$= 5 cycles roll-bonding, the thickness of layer was equal to $t_5$ = 1/32 mm = 31.25 μm, total reduction was $Z_5$ = 96.875 % and total equivalent deformation was $\varepsilon_5$ = 4; in the case of $n$ = 10 cycles of roll-bonding the final thickness of layer is equal to $t_{10}$ = 1/1024 mm = 0.98 μm, total reduction $Z_{10}$ = 99.9 % and total equivalent deformation $\varepsilon_{10}$ = 8 can be obtained.

Although relatively large deformation can be obtained, in practice the end parts of strip have to be prepared each time after roll-bonding and then, with increasing number of cycles, the length of roll-bonded strip decreases.

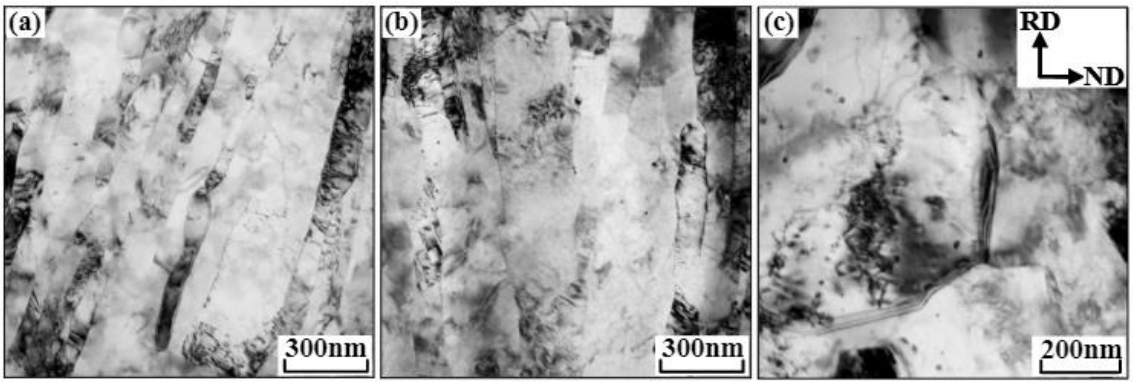


*Fig. 10. TEM images of the Cu-Cr-Zr alloy processed by ARB: (a) 5 cycles, (b) 5 cycles followed by aging at 450 ºC for 2 ks, (c) 5 cycles followed by aging at 450 C for 2 ks (higher magnification) [26].*

It should be noted that SPD processing is not limited just to these three methods. There are other numerous SPD processing techniques, and their full list can be found in the very recent review article [27].

## 1.3. Properties of UFG materials

The fabrication of bulk samples and billets using ECAP, HPT, ARB and other SPD techniques was a crucial first step in initiating investigations into the properties of bulk nanomaterials because the use of SPD processing permitted, and subsequently fully supported, a series of systematic studies using various nanostructured metallic materials including commercial alloys. The research works include strength and strengthening mechanisms, ductility and ways to its enhancement, fatigue and wear resistance. The main achievements of these studies are discussed in the Section below.

### 1.3.1. Strength

Although the mechanical and functional properties of all polycrystalline metallic materials are determined by several factors, the grain size of the material generally plays the most significant and often a dominant role. Thus, the strength of different polycrystalline materials is related to the grain size, *d*, through the Hall-Petch equation which states that the yield stress, $\sigma_y$, is given by

$$\sigma_y = \sigma_o + k_y d^{-1/2} \qquad (9)$$

where $\sigma_o$ is termed the friction stress and $k_y$ the Hall-Petch constant [28, 29]. It follows from the equation that the strength increases with a reduction in the grain size and this has led to an ever-increasing interest in fabricating materials with extremely small grain sizes.

Significant body of experimental research has shown that grain size hardening is the most effective strengthening mechanism in the UFG and NS metallic materials. However, it should be noted that inverse Hall-Petch behaviour can be observed in nanocrystalline metals as was reported for nanocrystalline Cu and Pd [3]. Investigations showed that in the NS metals with grain size below ~100 nm, grain boundary mediated mechanisms may start to play an important role in the plastic deformation degrading the grain size strengthening. So, the Hall-Petch slope $k_y$ is generally expected to decrease in metallic materials when grains are smaller than~100nm. This effect has been referred to as a negative deviation from the Hall-Petch law [28, 29]. For instance from an experiment of an Al alloy we can see from Fig. 11a that proof strength shows a linear relationship with $d^{-1/2}$ in the AA1100 and the binary Al alloy (Al–3%Mg) both having grain size decreasing down to 200 nm. So, it can be concluded that the Hall–Petch concept is generally valid for the UFG Al alloys, as well. However, it should be noted that the Hall–Petch law does not take into account neither grain boundary characteristics, nor possible activation of deformation mechanisms other than the dislocation pileup mechanism related to the ultra-fine grains.

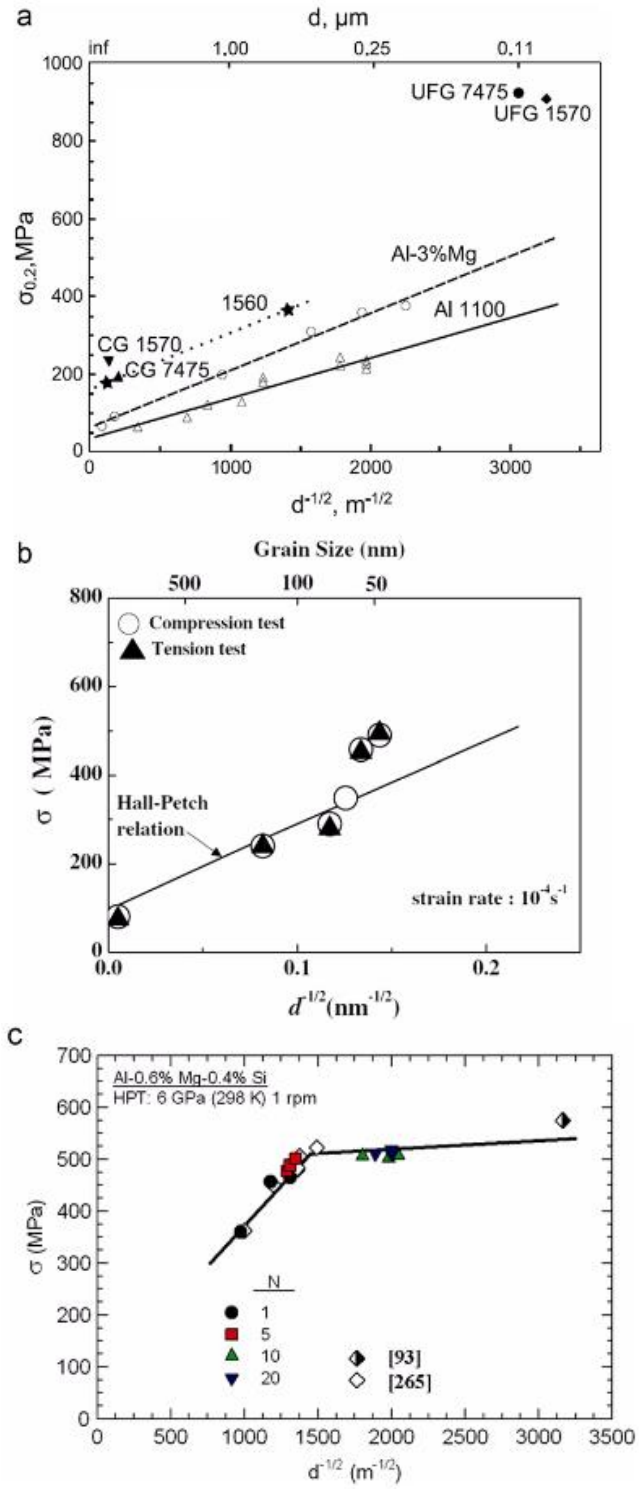


*Fig. 11. The Hall–Petch relationship for: (a) AA1100, Al–3%Mg, AA1570, and AA7475 [30]; (b) pure Al (99.5 wt%) [31]; (c) Al–0.6%Mg–0.4%Si [32].*

.

### 1.3.2. Tensile Ductility

High ductility in metallic materials is another very important property for their structural use. It is essential for metal-forming operations as well as to avoid catastrophic failure in load-bearing applications during their service life. The ductility of materials is defined as the extent to which a material can be plastically deformed. Two measures of ductility will be considered below. First, uniform elongation is the maximum strain where homogeneous plastic flow (uniform reduction of cross-sectional area) is still observed and beyond which a diffuse necking begins. The uniform elongation is determined by competition between plastic flow and materials resistivity to macro-localization of plastic flow. It can be important in stretch-metal-forming operations. The second measure, elongation to failure (often referred to as total elongation to fracture or engineering strain at fracture), is a sum of uniform elongation and necking elongation. The latter is controlled by competition between localized plastic flow and fracture processes.

It has been a long-standing goal for materials scientists to synthesize structural materials with balanced combinations of high strength and high ductility. However, during the last decade, it has been widely demonstrated that a major grain refinement, down to the nanometer range, may lead to a very high hardness and strength in various metals and alloys, but nevertheless these materials invariably exhibit low ductility under tensile testing. A similar tendency is well known for metals subjected to heavy straining by other processes such as rolling, extrusion or drawing. Strength and ductility are the key mechanical properties of any material but these properties typically have opposing characteristics. Thus, materials may be strong or ductile but they are rarely both. The reason for this dichotomy is of a fundamental nature. Indeed, the plastic deformation mechanisms associated with the generation and movement of dislocations may not be effective in ultrafine grains. This is generally equally true for SPD processed materials. Thus, most of these materials have a relatively low ductility but they usually demonstrate significantly higher strength than their coarse-grained counterparts. Despite this limitation, it is important to note that SPD processing leads to a reduction in the ductility which is generally less than in more conventional deformation processing techniques such as rolling, drawing and extrusion. For example, experiments were conducted to compare the strength and ductility of the AA3004 processed by ECAP and cold-rolling (CR) [33]. As illustrated by the data plotted in Fig. 12, the yield strength increased monotonically with the increasing equivalent strain imparted into the alloy by either CR or ECAP [34].

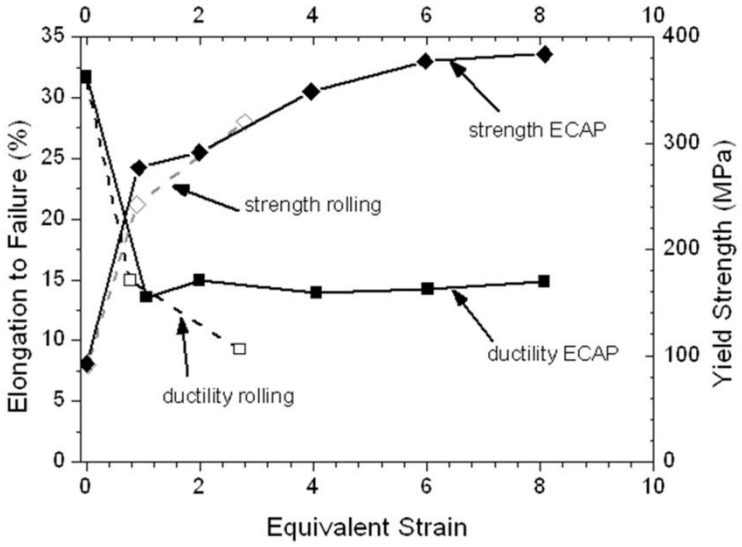


*Fig. 12. A comparison of yield strength and ductility for an Al-3004 alloy processed by cold-rolling or ECAP [34].*

However, it is apparent also that the overall ductility exhibits different trends for these two processing methods. After one ECAP pass, equivalent to a strain of ~1, the elongation to failure decreases from ~32 % to ~14 %. At the same time, there is no additional reduction in the ductility with additional ECAP passes. By contrast, CR decreases the ductility by a similar magnitude initially but thereafter the ductility continues to decrease with increasing rolling strain although at a slower rate. Consequently, ECAP processing of the alloy leads ultimately to a greater retention of ductility than conventional CR.

Typically in the nanostructured metallic materials, plastic deformation localizes at the very early stage of plastic deformation (1-3 %) resulting in necking, followed by a specimen failure. Various strategies to improve low ductility of the nanostructured metals and alloys have been proposed [35, 36, 37]. These strategies could be divided into two groups which we would define as (1) 'mechanical' strategies and (2) 'microstructural' strategies. The 'mechanical' strategies employ the mechanical characteristics of the UFG materials such as their work hardening ability and/or strain rate sensitivity. These mechanical characteristics can be varied by changing the testing parameters such as temperature and/or strain rate. The 'microstructural' strategies are based on the idea of intelligent microstructural design.

For tensile behaviour the uniform strain is usually in good agreement with the well-known Considère criterion [38],

$$\left(d\sigma / d\varepsilon\right) = \sigma \qquad (10)$$

which is a geometric criterion stating that when the work hardening rate, ($d\sigma/d\varepsilon$), decreases to the level of the flow stress, $\sigma$, macro-localization of plastic deformation (necking) should occur resulting in a specimen failure. The nanostructured metallic materials are usually characterized by increased strain rate sensitivity even at low

temperatures compared to their coarse-grained counterparts. Therefore, the Hart criterion [39] is more appropriate to predict the uniform elongation of the nanostructured metals and alloys:

$$(d\sigma / d\varepsilon) = (1 - m)\sigma \qquad (11)$$

Where $m$ is strain rate sensitivity index. It follows from the equation that the uniform elongation can be enhanced by (1) increasing the work hardening rate $d\sigma/d\varepsilon$ and/or (2) the strain rate sensitivity $m$.

Meanwhile, since the mechanical characteristics of the materials are also determined by their microstructure, it can be outlined that manipulation with the microstructure is the major tool to enhance the ductility of the nanostructured alloys.

In this connection, findings of extraordinary high strength and good ductility in several bulk UFG metals produced by SPD are of special interest. It is important to consider in detail the three different approaches that were used in the earlier investigations.

In the first study, high purity (99.996%) Cu was processed at room temperature using ECAP with a 90° clockwise rotation around the billet axis between consecutive passes in route $B_C$ [40]. The strength and ductility were measured by uni-axial tensile tests, and the resulting engineering stress–strain curves are shown in Fig. 13 for the Cu samples tested at room temperature in the initial coarse-grained condition and in three processed states. It is apparent that the initial coarse-grained Cu with a grain size of about 30 μm has a very low yield stress with significant strain hardening and a large elongation to failure. CR of the Cu with reduction ratio of 60% significantly increases the strength (curve 2 in Fig. 13), but dramatically decreases the elongation to failure. This result is consistent with the classical mechanical behaviour of metals that are plastically deformed. The same tendency is true also for Cu subjected to two passes of ECAP. However, further straining of Cu to 16 passes of ECAP (curve 4 in Fig. 13) simultaneously increases both the strength and ductility. Furthermore, the increase in ductility is much more significant than the relatively minor increase in strength.

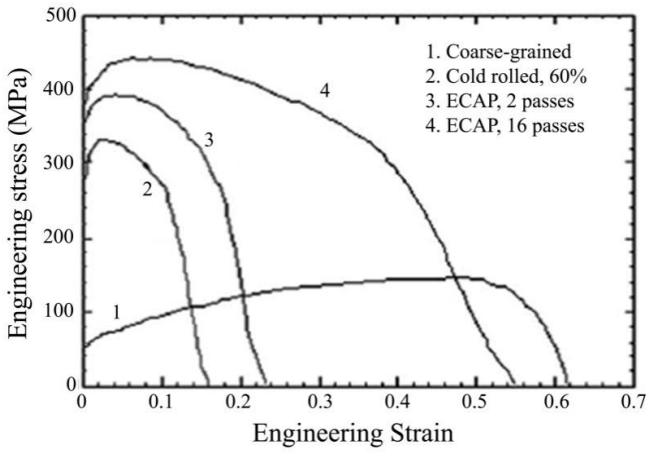


*Fig. 13. Tensile engineering stress–strain curves for Cu tested at 22 °C with a strain rate of $10^{-3}$ $s^{-1}$: the processing conditions for each curve are indicated.*

Thus, the data shown in Fig. 13 for ECAP processed Cu clearly demonstrate an enhancement of strength as well as ductility with accumulated deformation due to an increase in the number of passes from 2 to 16. This is a very remarkable result that for the first time was observed in metals processed by plastic deformation.

### 1.3.3. Functional properties

#### 1.3.3.1. Electrical conductivity

Pure copper features excellent electrical properties, which makes it attractive for a number of industrial fields. However, its low mechanical strength is a limiting factor for many applications. To improve the strength of pure metals, many approaches can be considered, for instance alloying to form solid solution and/or second phase particles, grain boundaries or dislocation strengthening. Unfortunately, each of these approaches has a negative impact on electrical conductivity. Therefore, there is a need to compromise these two properties. Cu-Cr-Zr alloys are an example of combining mechanical strength and electrical conductivity on a very high level. Their mechanical properties are much higher than for pure copper because of the addition of alloying elements, which form precipitates during ageing of water quenched supersaturated solid solution. A very high electrical conductivity is assured by low solubility of Cr and Zr in copper matrix at room temperature [41]. Cu-Cr-Zr alloys are used as electrical wires or trolley wires for fast railway. Due to the combination of excellent mechanical strength with very high electrical as well as thermal conductivity, they are considered as a prime material for fusion reactors, e.g. international thermonuclear experimental reactor, ITER [42, 43]. An additional advantage of these materials is the possibility to tailor their properties using different heat treatments and manufacturing processes involving almost every known strengthening mechanisms.

The strength of Cu-Cr-Zr alloys can be improved by increasing the content of alloying elements. However, this causes difficulties in manufacturing process as well as a decrease in electrical conductivity. In this work, an attempt has been made to improve mechanical strength of a Cu-Cr-Zr alloy while maintaining its high electrical conductivity without changing chemical composition. This can be obtained by using severe plastic deformation (SPD) techniques. They are known as an effective way of grain size refinement below 1 micron and the production of ultrafine grained (UFG) materials. Such materials feature extremely high strength due to grain boundaries strengthening as described quantitatively by the Hall-Petch relationship [28, 29]. Nowadays, the most popular SPD techniques include ECAP [44] HPT [45]. Also, Hydrostatic Extrusion (HE) was proved to be an efficient method of grain size refinement [46].

Satisfactory combination of high mechanical properties and good electrical conductivity is possible employing processes which lead to precipitation hardening and grain refinement. Both of them cause the scattering of electrons, which results in a decrease in electrical conductivity comparing to pure solvent metal. Nonetheless this drop is significantly smaller than the one caused by solid solution. The precipitates even increase

the electrical conductivity of the alloy after age hardening. Age hardening combined with SPD processing make it possible to obtain a material with very high mechanical properties together with relatively high electrical conductivity which can be attractive for many industrial applications.

**ITER**

The production of electrical energy from nuclear fusions is currently highly advanced field of the interest in an international scientific cooperation in the International Thermonuclear Experimental Reactor programme (ITER). Alloys based on Cu are used in the ITER project however from the future perspective in terms of the physical and mechanical properties improvement, the alloy based on Cu-Cr-Zr is proposed. The Cu-Cr-Zr alloy is classified as a precipitation-hardened material which is used as a functional material for various applications in ITER, for example the first wall, blanket and support, divertor and heating systems. In this study, as an experimental material was used Cu-Cr-Zr alloy with the chemical composition of 98.54 wt.% Cu, 1.1 wt.% Cr, 0.043 wt.% Zr and 0.317 wt.% impurities. There was used ECAP method and heat treatment to enhance the strength properties in Cu-Cr-Zr alloy. The application of sophisticated treatments based on solution annealing, structure formation by ECAP on nanoscale level and additional artificial ageing producing precipitation strengthening can be achieved the yield strength more than 500 MPa.

In the present study, there is used ECAP method and heat treatment to enhance the strength properties in Cu-Cr-Zr alloy. According to this study, following conclusions can be made: • on the essential electricity consumption prognosis for to 21 century should be assumed that in 2080 year will be necessary reach electricity power 100 TWh,

• This electricity power will be achieve by “pure sources” there are considered pure fossils, renewable resources and nuclear fusion,

• The very effective and perspective pure source is appears nuclear fusion,

• Nuclear fusion is running in thermonuclear reactor for which must be selected special grades of metal materials,

• One special grades of metal material is precipitation hardening Cu-Cr-Zr alloy,

• Today research orientation is preparing processing conditions leading to maximalization of strength properties and weight reducing of construction elements,

• By sophisticated treatment of Cu-Cr-Zr alloy was obtained yield strength 0.2YS>500 MPa,

• Sophisticated treatments are based on two lines:

  • SA+1xECAP+AT=144 MPa (base level) + 236 MPa (effect from grain size refinement) + 124 MPa (effect from precipitation hardening) = 504 MPa,

  • SA+3xECAP=144 MPa (base level) + 388 MPa (effect from grain size refinement) = 532 MPa.

### 1.3.3.2. Wear behaviour

The variation in the weight loss of the different Cu–Cr–Zr alloys with the applied load is given in Fig.14. A diagram showing the variation of volume loss measured from the volume of worn tracks with the applied load is also included in the inset of Fig.14 in order to verify the weight loss results. It is clearly seen that both diagrams demonstrate almost the same variation in each case and under all loads. The weight/volume loss increases almost linearly with increasing applied load for all conditions, and the increase is more pronounced at higher loads, which agrees well with previous investigations [47, 48, 49]. Under low loads, no significant weight/ volume loss was observed for any of the samples. The alloy after aging (process-2) revealed the lowest wear resistance. The ECAP processing after quenching (process-3) increased the wear resistance of the alloy considerably by decreasing the weight/volume loss due to the increase in strength and hardness after ECAP [50]. The aging of the UFG microstructure (process-4) resulted in further increase in the wear resistance. For all test conditions, the alloy after the two-step process of ECAP and aging exhibited the smallest weight/volume losses. Long-term wear tests under a load of 5N and at a sliding speed of 0.2ms$^{-1}$ were also performed to verify the effectiveness of the hardening procedures on the wear resistance of the alloy during prolonged periods. The results are summarized in Fig. 15. In the initial stages of the tests, all hardened samples showed similar weight losses, but the differences increased during prolonged periods. At a constant load, the weight loss increased almost linearly with sliding distance in each case. It is seen clearly that the quenched samples showed very high weight loss compared to the processed ones. All processes applied to the quenched samples brought about a considerable increase in wear resistance of the alloy. The two-step process of ECAP plus aging resulted in the highest wear resistance.

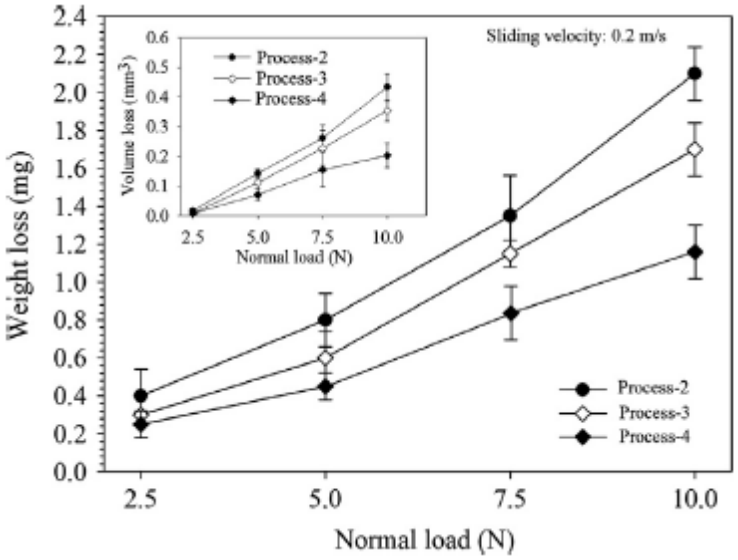

*Fig. 14. Variation in weight loss of the different Cu–Cr–Zr samples with applied load during dry sliding wear at room temperature. The variation in volume loss with applied load is also shown in the inset.*

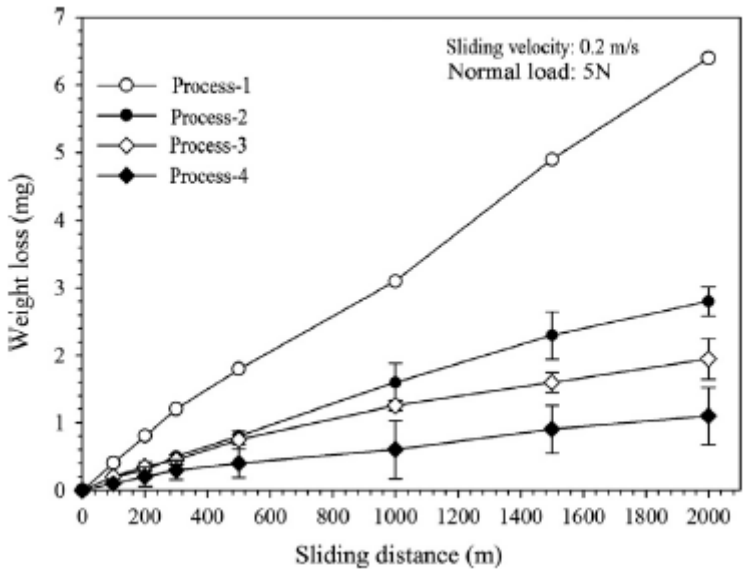


*Fig. 15. Variation in weight loss of the different Cu–Cr–Zr samples with sliding distance under a normal load of 5N during dry sliding wear at room temperature.*

### 1.3.3.3. Corrosion behaviour

There is a significant body of research regarding the effect of grain refinement on the corrosion properties of the Al alloys [51 - 62]. The fundamentals of the effect of grain size on corrosion behaviour in different metallic materials were discussed in overview [51]. Generally, studies of SPD processing on the chemical properties of the Al alloys are difficult because deformation processing imparts physical and chemical changes to the material in addition to the grain refinement (see Section 2). It can be outlined that nanostructured Al alloys show complex corrosion behaviour depending on the environment. The data in the literature can be separated into two classes [52]:

- Range of material-environment combinations showing low to passive corrosion rates ($\leq$10 μA $cm^{-2}$).
- Range of material-environment combinations exhibiting highly active corrosion rates ($\leq$10 μA $cm^{-2}$)

It was found that the data belonging to the first class tend to follow the Hall–Petch type law where corrosion resistance can be presented as:

$$i_{corr} = (A) + (B)d^{-1/2} \qquad (12)$$

where *A* is a function of the environment (as the same material with the same microstructure can have a different corrosion rate in different electrolytes), *B* is a material

constant determined by chemical composition of the material and its purity. This effect was experimentally observed on a wide range of metallic materials exhibiting some level of passivity (which have oxide on the metal surface). Fig. 16a illustrates this effect for pure Al with different average grain sizes achieved using different processing routes (ECAP, cryorolling, drawing, etc.) [52, 53]. This was related to the fact that grain refinement allows different rates of oxide growth on the surface. Since the oxide film conduction rate on surface is governed by grain boundary density, UFG structures are expected to be more corrosion resistant. In the absence of an oxide film on the surface (at dissolution rates of >>10 μA $cm^{-2}$), ultra-fine grained microstructures containing high grain boundary densities will enhance overall surface reactivity and, consequently, the corrosion rate (Fig. 16b).

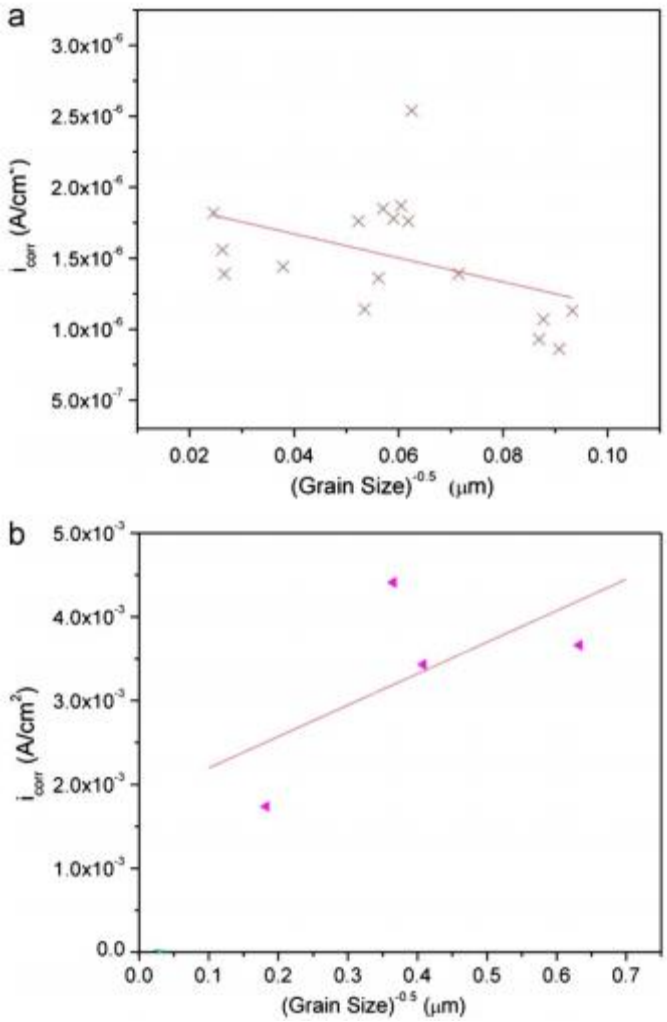


*Fig. 16. The relationship between the corrosion rate and grain size for: (a) low to passive current densities (pure Al) [51], (b) high current densities (AA6063) [63].*

Grain refinement can significantly affect also the local corrosion behaviour of the Al alloys. In [64], nanostructured Al–Mn alloy subjected to immersion in 3.5%NaCl artificial seawater for 168 h had fewer and finer pits compared to its coarse-grained counterpart due to more homogeneous surface energy distribution as well as due to the finer $Al_6Mn$ particles. An increased pit initiation resistance was reported also for Al–Mg

alloys and AA5083 subjected to short term corrosion testing [65], AA5052 [66], AA6082 [67], etc. However, the long term pit resistance of the nanostructured Al alloys shows an ambiguous character. The pitting depth in the nanostructured Al–Mg alloys was larger than that in the conventional material and also varied with varying Mg content. This effect was related to susceptibility of the nanostructured Al alloys to intergranular corrosion (Fig. 17) whereas their coarse-grained counterparts are non-susceptible.

It should be noted that no research activities on corrosion behaviour of Cu-Cr-Zr alloys have been carried out up to date.


*Fig. 17. SEM micrograph of the nanostructured Al–8.6Mg alloy after 6 months of alternate immersion in 3.5%NaCl in the 50%YS condition. Inside the pit intergranular corrosion is obvious [68].*

### 1.3.3.4. Strain-controlled fatigue

Since the cyclic response of the material under investigation is qualitatively similar for the specimens subjected to different ECAP followed by aging treatments we shall illustrate most important features of their cyclic behaviour on the specimens pressed 8 times through the dies and then aged at 500°C for 1 h, Fig. 18. Progressive cyclic softening occurs at all plastic strain amplitudes applied and in all aged specimens tested including reference commercial Cu–Cr. The rate of softening is slightly dependent on the plastic strain amplitude, increasing with increasing $\Delta\varepsilon_{pl}/2$. Nevertheless, the

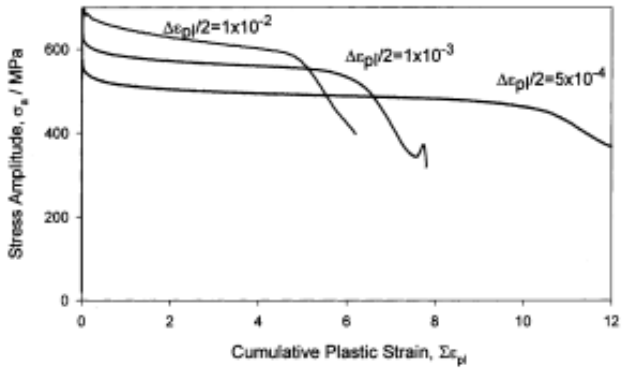


*Fig. 18. Cyclic response of ECAP Cu–Cr–Zr (8 passes, aged at 500°C, 1 h) tested under different $\Delta\varepsilon_{pl}/2$. Plastic strain amplitudes are indicated on the graphs [69].*

susceptibility to softening is very sensitive to the thermo-mechanical history of the specimens. Fig. 19 demonstrates the cyclic hardening/softening curves for different specimens examined at the moderate plastic strain amplitude $\Delta\varepsilon_{pl}/2=10^{-3}$. One can see that the highest softening rate is demonstrated by the specimen that has received the largest amount of pre-strain (12 ECAP-passes) and aged at 375°C. We would like to emphasize that the as fabricated but not aged ECAP specimens do not soften, curve 1 in Fig. 19, despite intensive prestraining.

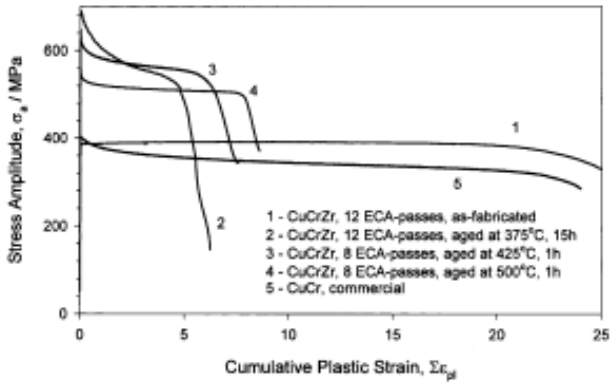


*Fig. 19. Cyclic hardening/softening curves for Cu–Cr–Zr and Cu–Zr alloys subjected to different thermo-mechanical treatments and tested under the same plastic strain amplitude $\Delta\varepsilon_{pl}/2=10^{-3}$ [69].*

This fact can serve as an evidence for a dominant role played by strengthening particles in cyclic softening of the materials under investigation. Fig. 17 also confirms that by changing aging conditions one can largely vary the cyclic response of dispersion hardenable alloys after ECAP. Although softening is visible in ECAP Cu–Cr–Zr, it should not be entirely associated with SPD fabrication, because this phenomenon is commonly observed in commercial Cu–Cr–Zr and Cu–Cr which did not receive such intensive pre-strain. The low-cyclic fatigue life dependence on the plastic strain amplitude obeys the Coffin–Manson law $\Delta\varepsilon_{pl}/2=\varepsilon(2Nf)^c$ with $\varepsilon_f$ the fatigue ductility and c the fatigue

exponent, both are materials constants, Fig. 20. Typically for many other SPD materials [53, 54], fatigue life of ECAP Cu–Cr–Zr is somewhat shorter than that of the reference commercial Cu–Cr material that emphasizes a key role of ductility in fatigue under strain control. Fatigue life of the ECAP specimens is the shortest in the under aged state (aging at 375°C). It is worth noting, that the slope of the Coffin–Manson line is the same for the reference Cu–Cr (c = -0.68) and for the as-fabricated ECAP alloy, while the fatigue exponent in the aged ECAP specimens is notably higher (c = -0.92 for the 8 ECA-pass Cu–Cr–Zr aged at 500°C 1 h) so that at high strain amplitudes greater than $10^{-2}$ the aged ECAP specimen may endure longer than its non-aged counterpart or commercial Cu–Cr. When comparing two different materials, Cu–Cr–Zr and Cu–Cr, one should also bear in mind that the latter material contains fewer amounts of strengthening secondary phases and precipitates. It is therefore less strong and more ductile, Fig. 18, which results in the smaller absolute value of the fatigue exponent and somewhat longer low-cyclic fatigue life. It is, however, undoubtedly shown that LCF properties of present Cu–Cr–Zr are in range of practical expectations, and these properties are variable through post-ECAP thermal treatment that helps to obtain a desired compromise in HCF and LCF performance.

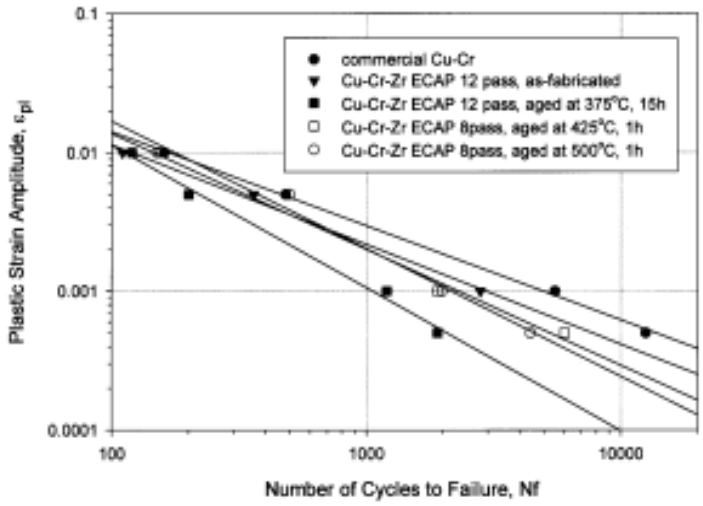


*Fig. 20. Coffin–Manson plots for materials under investigation [69].*

# 2 MOTIVATION AND OBJECTIVES

# 2. Motivation and objectives of the Final Degree Project

One can see from the first chapter of this thesis that there are a lot of studies on the UFG Cu-Cr-Zr alloys. These studies focused on strength, uni-axial tensile ductility, wear resistance, electrical conductivity of the material, and all these properties, apart from uni-axial tensile ductility, have been improved via grain refinement. Therefore, UFG Cu-Cr-Zr alloys appear as attractive materials for applications in various sectors of engineering. However, for fabrication of tools/parts from the UFG Cu-Cr-Zr alloys, in most of the cases they should undergo metalforming operations. The low uni-axial tensile ductility of the UFG materials can limit their formability, and, therefore, can be an obstacle for their commercialization.

In this project we are going to study uni-axial tensile properties of the UFG Cu-0.6Cr-0.08Zr and their correlation with biaxial stretching formability of the UFG material. The reason for that is it has been experimentally demonstrated that in UFG and NS metallic materials, mechanisms operating during plastic deformation under complex stress state might be different from those operating during uni-axial homogeneous tensile deformation, thus resulting in enhanced formability of the UFG material deformed in complex strain path. Special attention is also paid to the strain rate sensitivity of the UFG Cu-Cr-Zr alloy in uni-axial tensile testing and in biaxial stretching. This is due to the fact, that enhanced strain rate sensitivity can improve ductility of the UFG metallic materials according to the Hart criterion (see Section 1.3.2).

The main objectives of the present work were:

I. To fabricate UFG Cu-0.6Cr-0.08Zr alloy processed via two different ECAP processing routes;

II. To investigate the effect of SPD processing route on the microstructure;

III. To study mechanical behaviour and mechanical properties of the UFG Cu-0.6Cr-0.08Zr alloy deformed in uni-axial tensile mode and bi-axial stretching;

IV. To understand the effect of microstructure and deformation mode on uni-axial tensile ductility and biaxial stretching formability of the UFG Cu-0.6Cr-0.08Zr alloy.

# 3 MATERIALS AND EXPERIMENTAL PROCEDURES

# 3. Materials and experimental procedures

## 3.1. Material and processing

A Cu-0.6Cr-0.08Zr alloy was chosen as a material for this investigation. Information on impurity content of the material can be found in *Table 1*. The alloy was supplied by National Bronze (Lorain, Ohio, USA) in form of rods having a diameter of 10 mm. These rods were cut into smaller bars having a length of 100 mm and the same diameter, which were solution treated at 980 ºC for 1 h and quenched in water.

Table 1. Information on impurity content of the studied alloy.

| Cr | Zr | P | Si | Fe | TOI | Cu |
|---|---|---|---|---|---|---|
| 0.6 | 0.08 | 0.018 | 0.010 | 0.012 | <0.05 | Remaining |

The solution treated bars were subjected to equal channel angular pressing (ECAP) at room temperature via route Bc. Schematic presentation of the ECAP technique is shown in *Fig. 21*.

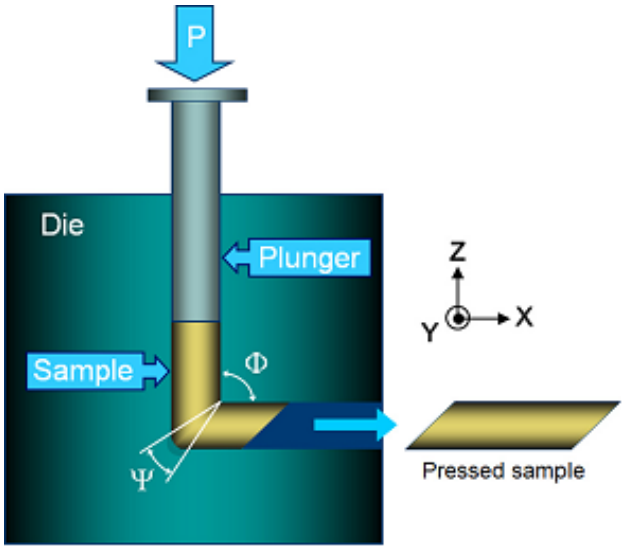


*Fig. 21. Schematic presentation of the ECAP die.*

The first batch of bars was ECAP processed using die with an angle Φ = 90º for 8 passes, whereas another batch of bars was processed in the die with an angle Φ = 110º. for 8 passes. The arc curvature angle was 0º in both dies.

$$\varepsilon_N = \frac{N}{\sqrt{3}}\left[2\,cot\,(\frac{\Phi}{2}+\frac{\psi}{2}) + \Psi cosec(\frac{\Phi}{2}+\frac{\psi}{2})\right] =$$

For ECAP Φ = 110º. $\varepsilon_N$ = 6.5

For ECAP Φ = 90º. $\varepsilon_N$ = 9.2

## 3.2. Microstructural characterization

### 3.2.1. Optical microscopy

An optical microscope works very much like a refracting telescope, but with some minor differences. Let's briefly review how a telescope works.

A telescope must gather large amounts of light from a dim, distant object; therefore, it needs a large objective lens to gather as much light as possible and bring it to a bright focus. Because the objective lens is large, it brings the image of the object to a focus at some distance away, which is why telescopes are much longer than microscopes. The eyepiece of the telescope then magnifies that image as it brings it to your eye.

*Fig. 22. View of optical microscope.*

In contrast to a telescope, a microscope must gather light from a tiny area of a thin, well-illuminated specimen that is close-by. So the microscope does not need a large objective lens. Instead, the objective lens of a microscope is small and spherical, which means that it has a much shorter focal length on either side. It brings the image of the object into focus at a short distance within the microscope's tube. The image is then magnified by a second lens, called an ocular lens or eyepiece, as it is brought to your eye.

The other major difference between a telescope and a microscope is that a microscope has a light source and a condenser. The condenser is a lens system that focuses the light from the source onto a tiny, bright spot of the specimen, which is the same area that the objective lens examines.

Also unlike a telescope, which has a fixed objective lens and interchangeable eyepieces, microscopes typically have interchangeable objective lenses and fixed eyepieces. By

changing the objective lenses (going from relatively flat, low-magnification objectives to rounder, high-magnification objectives), a microscope can bring increasingly smaller areas into view light gathering is not the primary task of a microscope's objective lens, as it is a telescope's.

To analyze the microstructure of the coarse-grained Cu-0.6Cr-0.08Zr alloy, we have ground the sample using grinding papers P600, P1200 and P2000. Then, the surface was polished using diamond paste 9 μm, 3 μm and 1 μm. Polishing with OPS was performed at the final stage so the final surface was a mirror-like. Finally, the surface was chemically attacked using etchant for 10 s. The chemical solution of the etchant was: 100-120 ml ethanol, 25 ml HCl and 7.5 g $Fe_3Cl$.

### 3.2.2. Transmission electron microscopy

The transmission electron microscope (TEM) operates on the same basic principles as the light microscope but uses electrons instead of light. What you can see with a light microscope is limited by the wavelength of light. TEMs use electrons as “light source” and their much lower wavelength make it possible to get a resolution a thousand times better than with a light microscope.

You can see objects to the order of a few angstroms ($10^{-10}$m). For example, you can study small details in the cell or different materials down to near atomic levels. The possibility for high magnifications has made the TEM a valuable tool in both medical, biological and materials research [70].

**Magnetic Lenses Guide the Electrons**

A "light source" at the top of the microscope emits the electrons that travel through vacuum in the column of the microscope. Instead of glass lenses focusing the light in the light microscope, the TEM uses electromagnetic lenses to focus the electrons into a very thin beam. The electron beam then travels through the specimen you want to study. Depending on the density of the material present, some of the electrons are scattered and disappear from the beam. At the bottom of the microscope the unscattered electrons hit a fluorescent screen, which gives rise to a "shadow image" of the specimen with its different parts displayed in varied darkness according to their density. The image can be studied directly by the operator or photographed with a camera.

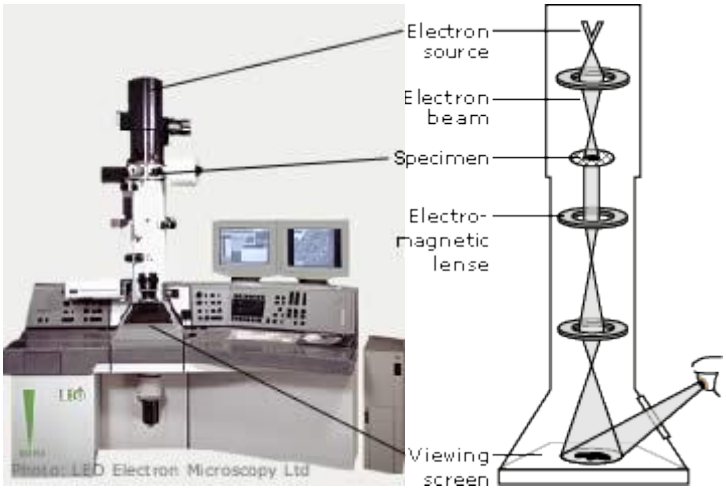


*Fig. 23. View of transmission electron microscope.*

**Source formation.**

From the top down, the TEM consists of an emission source, which may be a tungsten filament, or a lanthanum hexaboride ($LaB_6$) source. For tungsten, this will be of the form of either a hairpin-style filament, or a small spike-shaped filament. $LaB_6$ sources utilize small single crystals. By connecting this gun to a high voltage source (typically ~100–300 kV) the gun will, given sufficient current, begin to emit electrons either by thermionic or field electron emission into the vacuum. This extraction is usually aided by the use of a Wehnelt cylinder. Once extracted, the upper lenses of the TEM allow for the formation of the electron probe to the desired size and location for later interaction with the sample.

Manipulation of the electron beam is performed using two physical effects. The interaction of electrons with a magnetic field will cause electrons to move according to the left hand rule, thus allowing for electromagnets to manipulate the electron beam. The use of magnetic fields allows for the formation of a magnetic lens of variable focusing power, the lens shape originating due to the distribution of magnetic flux. Additionally, electrostatic fields can cause the electrons to be deflected through a constant angle. Coupling of two deflections in opposing directions with a small intermediate gap allows for the formation of a shift in the beam path, this being used in TEM for beam shifting, subsequently this is extremely important to STEM. From these two effects, as well as the use of an electron imaging system, sufficient control over the beam path is possible for TEM operation. The optical configuration of a TEM can be rapidly changed, unlike that for an optical microscope, as lenses in the beam path can be enabled, have their strength changed, or be disabled entirely simply via rapid electrical switching, the speed of which is limited by effects such as the magnetic hysteresis of the lenses.

**Optics**

The lenses of a TEM allow for beam convergence, with the angle of convergence as a variable parameter, giving the TEM the ability to change magnification simply by

modifying the amount of current that flows through the coil, quadrupole or hexapole lenses [71]. The quadrupole lens is an arrangement of electromagnetic coils at the vertices of the square, enabling the generation of a lensing magnetic fields, the hexapole configuration simply enhances the lens symmetry by using six, rather than four coils.

Typically a TEM consists of three stages of lensing. The stages are the condensor lenses, the objective lenses, and the projector lenses. The condensor lenses are responsible for primary beam formation, while the objective lenses focus the beam that comes through the sample itself (in STEM scanning mode, there are also objective lenses above the sample to make the incident electron beam convergent). The projector lenses are used to expand the beam onto the phosphor screen or other imaging device, such as film. The magnification of the TEM is due to the ratio of the distances between the specimen and the objective lens' image plane. Additional quad or hexapole lenses allow for the correction of asymmetrical beam distortions, known as astigmatism. It is noted that TEM optical configurations differ significantly with implementation, with manufacturers using custom lens configurations, such as in spherical aberration corrected instruments, or TEMs utilising energy filtering to correct electron chromatic aberration.

To study the microstructure of the Cu-0.6Cr-0.08Zr alloy, a JEOL-2100 microscope was employed operating at 200 kV. Samples for TEM study were prepared by twin jet electropolishing with a chemical solution consisting of 30% nitric acid and methanol at −15 ◦C and 15 V. Observations were made in both the bright and the dark field imaging modes, and selected area electron diffraction (SAED) patterns were recorded from areas of interest using an aperture of 1 μm nominal diameter.

### 3.2.3. Scanning electron microscopy

Scanning electron microscopy (SEM) can be defined as a microscopy technique that uses electrons instead of light to form an image. Since its development in the early 1950's, the SEM has been a powerful instrument widely used in materials science [58]. In SEM, a beam of electrons is produced by the electron gun. Then, it is focused on a specimen and scanned long a pattern of parallel lines. The purpose of the electron gun is to provide a stable beam of electrons of adjustable energy, which is held within vacuum. The beam travels through electromagnetic fields and lenses, which focus the beam down towards the sample. Once the beam hits the sample, electrons and X-rays are ejected from the sample. Various signals are generated as a result of the impact of the incident electrons: secondary electrons, high-energy backscattered electrons and characteristic X-rays

Detectors collect these X-rays, backscattered electrons, and secondary electrons and convert them into a signal that is sent to a screen in order to produce the final image Useful information can be obtained from the interaction between electrons and sample surface, such as the surface topography, composition and crystallography.

Specimens for microstructural characterization were ground and polished to a mirror-like surface using standard metallographic techniques. For SEM characterization, specimens were etched with 2 vol.% $HNO_3$ in ethanol (nital 2%) solution. Examination of the

microstructure was performed using a SEM EVO MA15 (Carl Zeiss, Oberkochen, Germany) operating at an accelerating voltage of 20 kV.

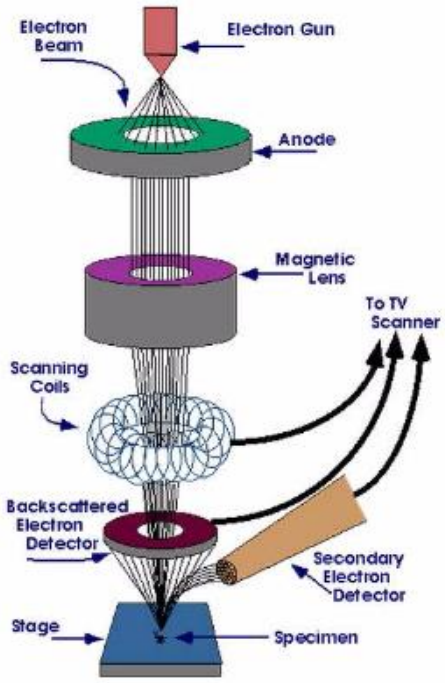


*Fig. 24. SEM schematic view.*

### 3.2.4. Electron backscatter diffraction characterization

Electron backscatter diffraction (EBSD) is a SEM based technique very useful for microstructural characterization and analysis of crystalline materials [72, 73]. It allows the micro-texture [74], grain and phase boundary characterization [75, 76], phase identification [77] and strain determination [78] in crystalline materials of any crystal structure.

The heart of the EBSD technique is the indexation of diffracted patterns that are obtained by focusing an electron beam on a crystalline sample. The sample is usually oriented at 70° (see Fig. 25) with respect to the horizontal plane which allows more electrons to be scattered and to be registered by the detector. The electrons disperse beneath the surface, subsequently diffracting among the crystallographic planes, according to Bragg's law. The diffracted signal is collected and viewed via a low-light video camera interfaced to a phosphor screen. If the sample produces good diffraction patterns, orientation determination is a three step process consisting of (i) Kikuchi band detection, (ii) Kikuchi band identification and (iii) determination of orientation. In the first step, Kikuchi band detection is carried through Hough Transform, by converting Kikuchi lines from recorded image into single points in the Hough space. In the second step, Kikuchi band identification is related to correct identification of the particular lattice plane associated with the reconstructed Kikuchi band. The width of detected bands is a function of the spacing of diffracting planes (Bragg's law) and is compared with a theoretical list of diffracting lattice planes. Additionally, the angles between bands have to be determined

and compared with theoretical values. This is done by comparison with a stored table in the database consisting of all interplanar angles between the low Miller indices planes (hkl) present in the crystal structure, including every individual plane in the family of planes {hkl}. In the third step, orientation determination is based on the calculation of the orientation of the corresponding crystal lattice with respect to the reference frame.

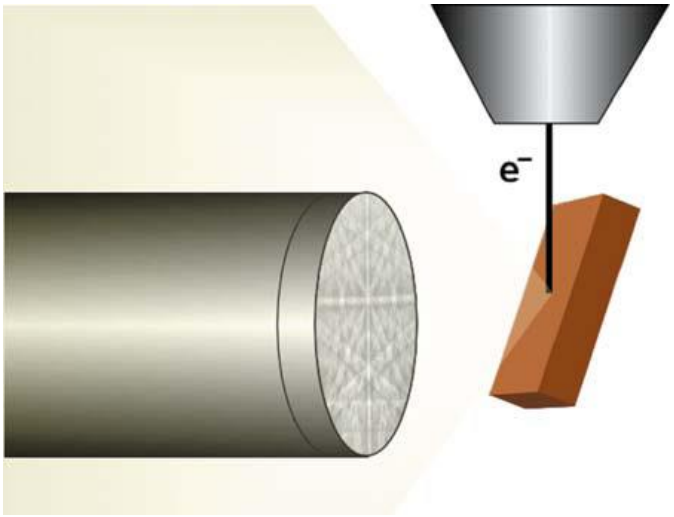


*Fig. 25. Schematic representation of the typical EBSD geometry, showing the pole piece of the SEM, the electron beam, the tilted specimen, and the phosphor screen [79].*

The diffraction patterns provide crystallographic information that can be related to their origin position on the specimen. Evaluation and indexing of the diffraction patterns is performed in most cases automatically and the data is output in a variety of both statistical and pictorial formats. The most versatile and revealing of these outputs is the "orientation map" (often called and Orientation Imaging Micrograph, OIM), which is a quantitative depiction of an area of the microstructure in terms of its crystallographic constituents. One common map constructed from EBSD data is the image quality (IQ) map. In such cases, electrons are diffracted from near the surface of the sample and the IQ can be considered as a metric describing the quality of a diffracted pattern. An IQ map is constructed by mapping the IQ value measured for each diffraction pattern obtained during an OIM scan to a gray or colour scale. Both the "perfection" of the crystal lattice and the atoms present within the diffracting volume affect the IQ. Therefore, IQ provides useful complementary information about these features to the indexed crystallographic orientations.

Optimum specimen preparation is a fundamental requirement for an EBSD experiment. Inadequate specimen preparation will result in degraded diffraction patterns which feed through loss of data quality. In this work, specimens for EBSD analysis were prepared using standard metallographic techniques with final polishing with OP-U (colloidal silica) for 40 minutes. Due to low availability reasons, Orientation imaging microscopy (OIM) studies were performed using two different equipments: first, a FEI Quanta™ 450 FEG-

SEM (FEI Corporate, Oregon, USA) equipped with a Hikari detector controlled by the EDAX-TSL OIM-Data Collection (version 6.2®) software (EDAX, Mahwah, USA). The data were acquired at an accelerating voltage of 20 kV, a working distance of 16 mm, a tilt angle of 70° and a step size of 40 nm. The orientation data were post-processed with TSL-OIM Analysis 6.2© software (EDAX, Mahwah, USA). Secondly, a FEI Quanta™ Helios NanoLab 600i (FEI Corporate, Oregon, USA), equipped with a NordlysNano detector controlled by the AZtec Oxford Instruments Nanoanalysis (version 2.4®) software (Oxford Instruments, Abingdon, United Kingdom) was used. The data were acquired at an accelerating voltage of 18 kV, a working distance of 10 mm, a tilt angle of 70° and a step size of 55 nm. The orientation data were post-processed with HKL Post-processing Oxford Instruments Nanotechnology (version 5.1©) software (Oxford Instruments, Abingdon, United Kingdom).

Data clean-up routines can compensate in part for unsolved patterns. The post processing of the raw orientation data can be described as follows. First, a confidence index (CI) standardization with a minimum grain size of 4 pixels was applied. This clean up algorithm changes the CI of all points in a grain to the maximum CI found among all points belonging to that grain. Afterwards, the neighbour CI correlation algorithm was employed, which implies that if a particular point has CI below 0.1, then the CI of the nearest neighbours are checked to find the neighbour with the highest CI. The orientation and CI of the particular point are reassigned to match the orientation and CI of the neighbour with the maximum CI. Finally, if the majority of neighbours of a particular grain smaller than 4 pixels with a grain tolerance angle of 5º belong to the same grain, then the orientation of the particular grain is changed to match that of the majority grain, i.e. a grain dilation algorithm was applied. It should be noted that clean-up procedures must never be used as an alternative to obtaining the best and most representative diffraction patterns.

## 3.3. Mechanical testing

Once we have the three materials (Annealed, ECAP 90º and ECAP 110º) we start machining the dog-bone shaped specimens for uni-axial tensile testing and disks for small punch testing. The geometry of samples is provided below in Fig. 26. The thickness of tensile specimens is 0.8 mm; the thickness of the disk is 0.4 mm.

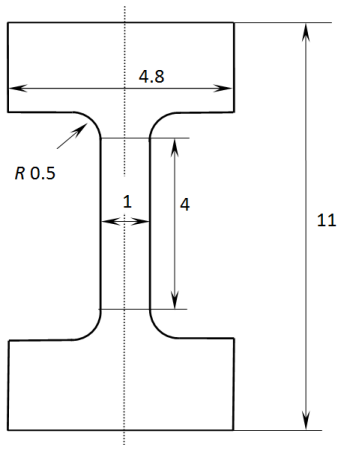


a

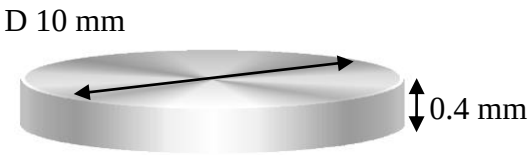


b

*Fig. 26. a) Geometry of dog bone shaped sample for uni-axial tensile testing; b) Geometry of disk for small punch testing.*

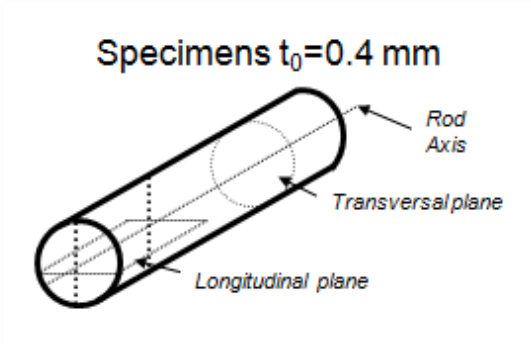


*Fig. 27. Bar sample.*

*Fig. 28. View of grinding papers.*

The machined samples were carefully ground using grinding paper P600 in one way. After that, we changed to grinding paper P1200 varying 90 degrees the grinding direction. At the final stage of grinding, we used the grinding paper P2000 to finish in the first direction that we used. While we were grinding, we checked the thickness of samples using precision thickness calliper (Fig. 29) until we obtained the needed one. The thickness of the prepared samples was homogeneous throughout the samples. The grinding process was carried out in a very gentle manner in order to avoid any additional deformation of the Cu alloy.

*Fig. 29. Precision thickness calliper.*

### 3.3.1. Uni-axial tensile testing

The engineering tensile test is widely used to provide basic design information on the strength of materials. In such test, a specimen is subjected to a continually increasing uni-axial tensile force while simultaneous observations are made of the elongation of the specimen until failure. The tensile force is recorded as a function of the increase in gage length. An engineering stress-strain curve can be subsequently constructed from the load-elongation measurement [80, 81]. Engineering stress is then defined as:

$$\sigma = F / A_0 \qquad (13)$$

where F is the tensile force and $A_0$ is the initial cross-sectional area of the gage section. Engineering strain is then defined as:

$$\varepsilon = \Delta L / L_0 \qquad (14)$$

where $L_0$ is the initial gage length and is the change in gage length ($L - L_0$). The advantage of dealing with stress versus strain rather than load versus elongation is that the stress-strain curve is virtually independent of the specimen dimensions [80, 81]. For most materials, the initial elastic portion of the curve is linear. The slope of this linear region is called the elastic modulus or Young's modulus [80, 81]:

$$E = \sigma / \varepsilon \qquad (15)$$

When the stress rises high enough values, the strain hardening behaviour will cease to be linear and the strain behaviour will not disappear completely on unloading. The strain that remains is called plastic strain. Once plastic deformation has begun, there will be both elastic and plastic contributions to the total strain. The onset of the plastic plasticity is usually described by an offset yield strength, which can be measured with greater reproducibility. It can be found by constructing a straight line parallel to the initial linear portion of the stress-strain curve, i.e. at 0.2% offset. The yield stress is then the stress at which this line intersects the stress-strain curve. The tensile strength (or ultimate strength) is defined as the highest value of the engineering stress-strain curve, i.e. the maximum load achieved divided by the original cross-sectional area of the specimen. Up to the maximum load, the deformation should be uniform along the gage section. In the case of ductile materials, such as steel, the tensile strength corresponds to the point at which the deformation starts to localize, forming a neck [80, 81]. There are two common measures used to describe the ductility of a material. First, the uniform elongation, εu, is the percentage of elongation at the point (stress) at which necking begins. Second, the elongation or engineering strain to fracture, εf, is the final strain value reached during test before failure [80, 81]. Another key property that can be determined from the engineering stress-strain curve is the strain-hardening exponent. Then value is given by the slope of a

graph of the logarithm of the true stress versus the logarithm of the true strain in the region of uniform elongation [80, 81].

Tensile tests were carried out using a Kammrath and Weiss tensile/compression module with 1 kN load cell at room temperature. The accuracy of load measurement was ± 0.1 N, whereas accuracy of measurements of displacement was ± 0.5 μm. The tensile tests were performed with constant cross head speed corresponding to two initial strain rates: $10^{-3}$ and $10^{-2}$ $s^{-1}$.

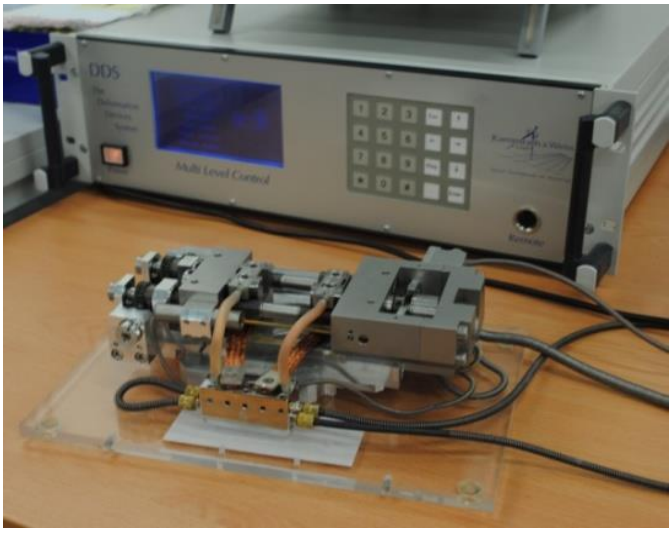

*Fig. 30. Tensile/compression module Kammrath&Weiss and controller.*

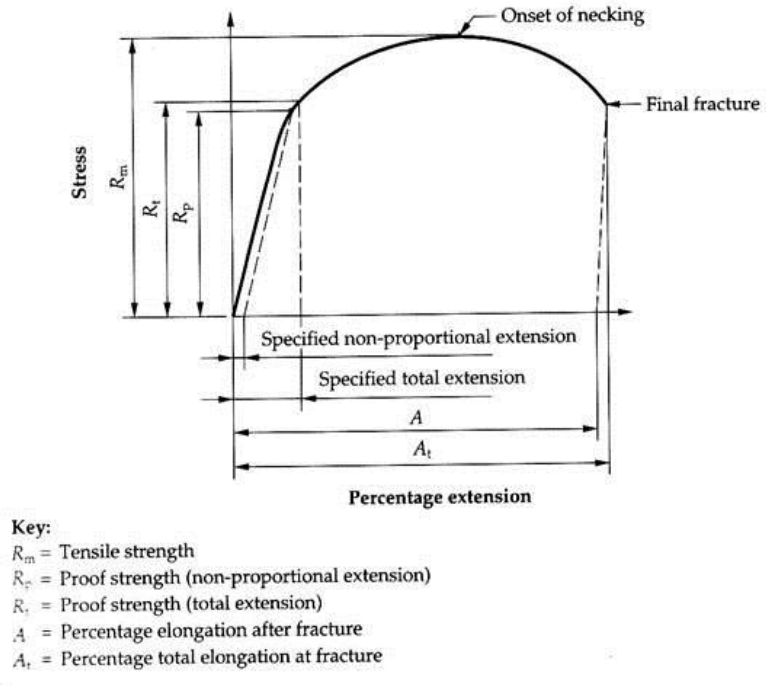


*Fig. 31. Schematic presentation of a typical engineering stress - strain curve from uni-axial tensile testing of a metal/alloy.*

To estimate the strain rate sensitivity index, m, strain rate jump tests were conducted at the base strain rate of $10^{-3}$ $s^{-1}$. The strain between the strain rate jumps (~0.03) was sufficient for possible transient effects associated with the inertia of the testing machine to die off. Strain rate jumps ($10^{-3}$ $s^{-1}$ → $10^{-2}$ $s^{-1}$ → $10^{-3}$ $s^{-1}$) were carried out. The *m*-values were calculated using the following standard equation [82]

$$m = \frac{\partial \ln(\sigma)}{\partial \ln(\dot{\varepsilon})} \equiv \frac{\ln(\sigma_2 / \sigma_1)}{\ln(\dot{\varepsilon}_2 / \dot{\varepsilon}_1)} \qquad (16)$$

where $\sigma_2$ and $\sigma_1$ are the values of the flow stress corresponding to the strain rates of $\dot{\varepsilon}_2$ and $\dot{\varepsilon}_1$, respectively. Back-extrapolation of the stress-strain curves to the strain at which a strain rate jump was made [82], was used to determine the $\sigma_2$ values and the instantaneous strain rate sensitivity.

### 3.3.2. Small-punch testing

Small punch testing (SPT) technique started its development at MIT on 1981 to study fragility on materials produced by radiation.

PT is nowadays used to determine mechanical tensile properties, formability, fracture and fluency behaviour as well as the study of any embrittlement phenomenon. Also due to the small punch test that uses is much appropriated for mechanical characterization of small zones. It will be impossible to do it with other methods. For example, for the thermal affected zones in the welds' joints [83, 84].

European Committee of Standardization coordinated by the European Pressure Equipment Research Council set a code of practice for application and use of small-punch tests as a tool for prediction of creep failure and toughness and properties of in-service materials. Small Punch Test (SPT) is a testing procedure which could being considered non destructive, on behalf of the so reduced size of the test tubes that uses, allows to rate directly mechanical properties of materials.

In the small punch test a disk like specimen is deformed in a miniaturized deep drawing experiment. The specimen is clamped between a die (bore diameter d=4 mm, die edge radius r=0.5 mm) and a down holder and centrically deformed by the punch with a

spherical head (radius R=1.2 mm). For irradiated material the device is put into a hot chamber. Small punch tests were carried out with the following punch speeds: 0.05 mm/min, 0.5 mm/min, and 5 mm/min.

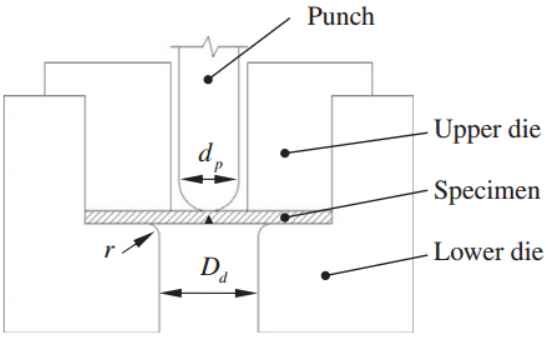


*Fig. 32. Schematic presentation of small punch testing.*

Small Punch Test (SPT) is a testing procedure which could being considered non destructive, on behalf of the so reduced size of the test tubes that uses, allows to rate directly mechanical properties of materials.

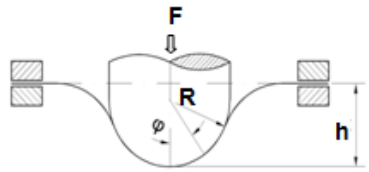


F: Punch load
h: Central deflection
R: Punch radius (1.2 mm)
Punch speed 0.5 mm/min

*Fig. 33. Geometry of tool for small punch testing.*

Fig. 34 shows the typical punch load-central deflection curve where all deformation stages are marked [85] Elastic bending is the first stage marked as I. This stage is related to the local surface micro-yielding. Plastic flow begins and spreads through punch-specimen contact area during plastic bending, stage II. Stage III corresponds to membrane (bi-axial) stretching. A flat specimen transforms into dome-shaped cup following the punch profile during this stage. It is considered that uniform deformation takes place along an annular section of specimen. Once maximum load is reached, unstable plastic flow onsets leading to formation of cracks and specimen failure.

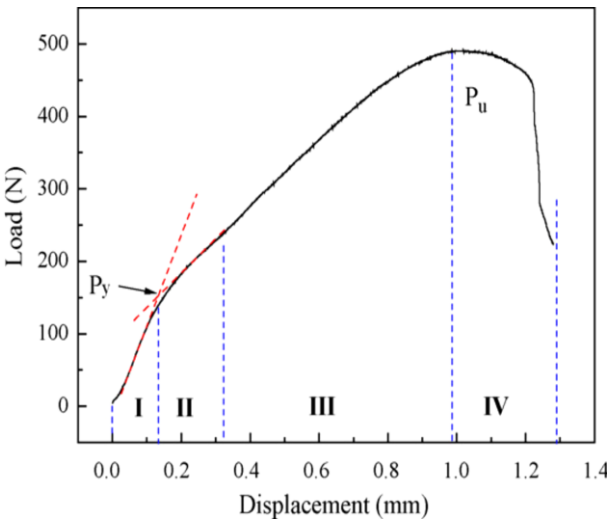


*Fig. 34. Typical punch load-displacement curve for 0.4 mm thickness small-punch specimen [85].*

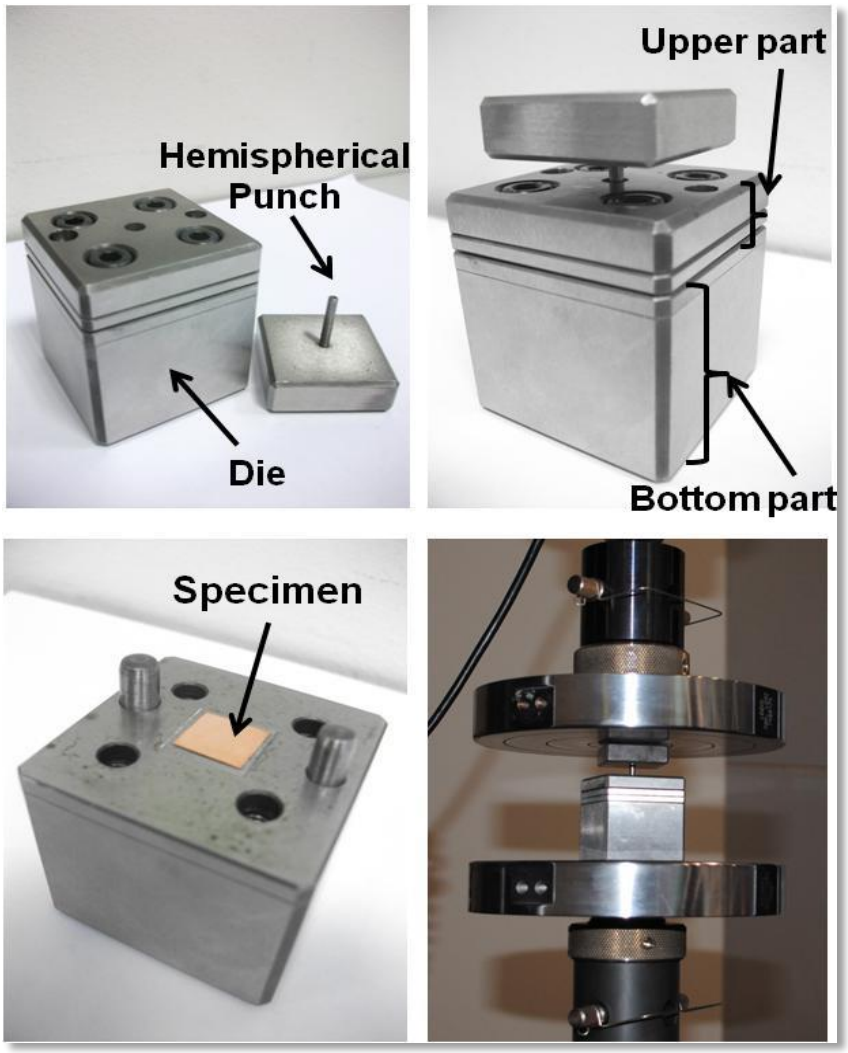

*Fig. 35. Experimental set-up for small punch testing used in this work.*

# 4 RESULTS AND DISCUSSIONS

# 4. Results and discussions

## 4.1. Effect of ECAP processing on microstructure of Cu-Cr-Zr alloy

### 4.1.1. Microstructure of the CG alloy

Figure 36 illustrates the microstructure of the coarse-grained Cu-0.6Cr-0.08Zr alloy. The grain size of the material was in the range of 50 to 300 μm with the average value of 122 μm. Annealing twins are seen in the coarse grains (marked by white arrows). Such annealing twins are typically present in the microstructure of the annealed pure Cu and its alloys.

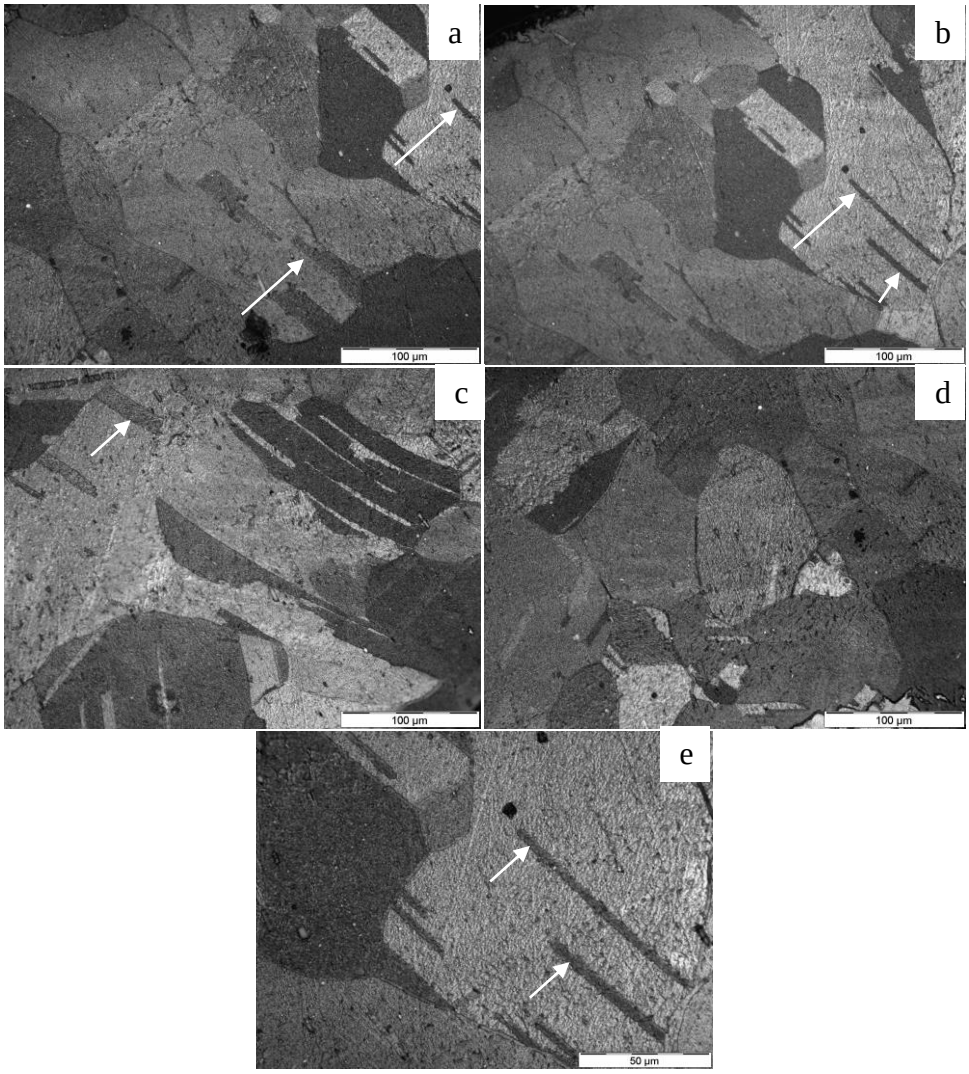


*Fig. 36. Optical microscopy images of the solution treated coarse-grained Cu-0.6Cr-0.08Zr alloy.*

### 4.1.2. Microstructure after ECAP 110º

Figure 37 shows transmission electron microscopy images of the microstructure of the Cu-0.6Cr-0.08Zr alloy after ECAP processing with a die having $\Phi$ =110º for 8 passes. Formation of complex microstructure is observed. Areas containing ultra-fine grains having a size of 100-200 nm are present along with the coarser grains having cell/subgrain structure in their interior. A typical cell is marked by white arrow in Fig. 37b, whereas an area with typical substructure (subgrains) is marked in Fig. 37d. Most of grains/subgrains are elongated. High dislocation density present in the microstructure should be also noted. It cannot be precisely estimated from TEM images, since individual dislocations cannot be clearly resolved due to their high density. It is well known, that SPD processed materials typically show high dislocation density up to $10^{14}$-$10^{15}$ $m^{-2}$ [3].

To perform more detailed quantitative analysis of the microstructure, EBSD measurements were carried out. Typical EBSD map for the Cu-0.6Cr-0.08Zr alloy after

ECAP processing with a die having $\Phi = 110^{o}$ for 8 passes in the Y plane (Fig. 1) is demonstrated in Fig. 38. The EBSD analysis confirms complex microstructure formed in the material after this ECAP processing. Majority of structural elements (such as grains or subgrains) have a size below 0.5 μm (Fig. 39). Most of grains/subgrains are elongated along the shear plane (Fig. 40) and have aspect ratio above 2. Profiles passed through the EBSD map clearly show that majority of grain boundaries have low misorientation (Fig. 41 and Fig. 42), that is also clearly indicated in the histograms of distribution of grain boundary misorientation presented in Fig 43.

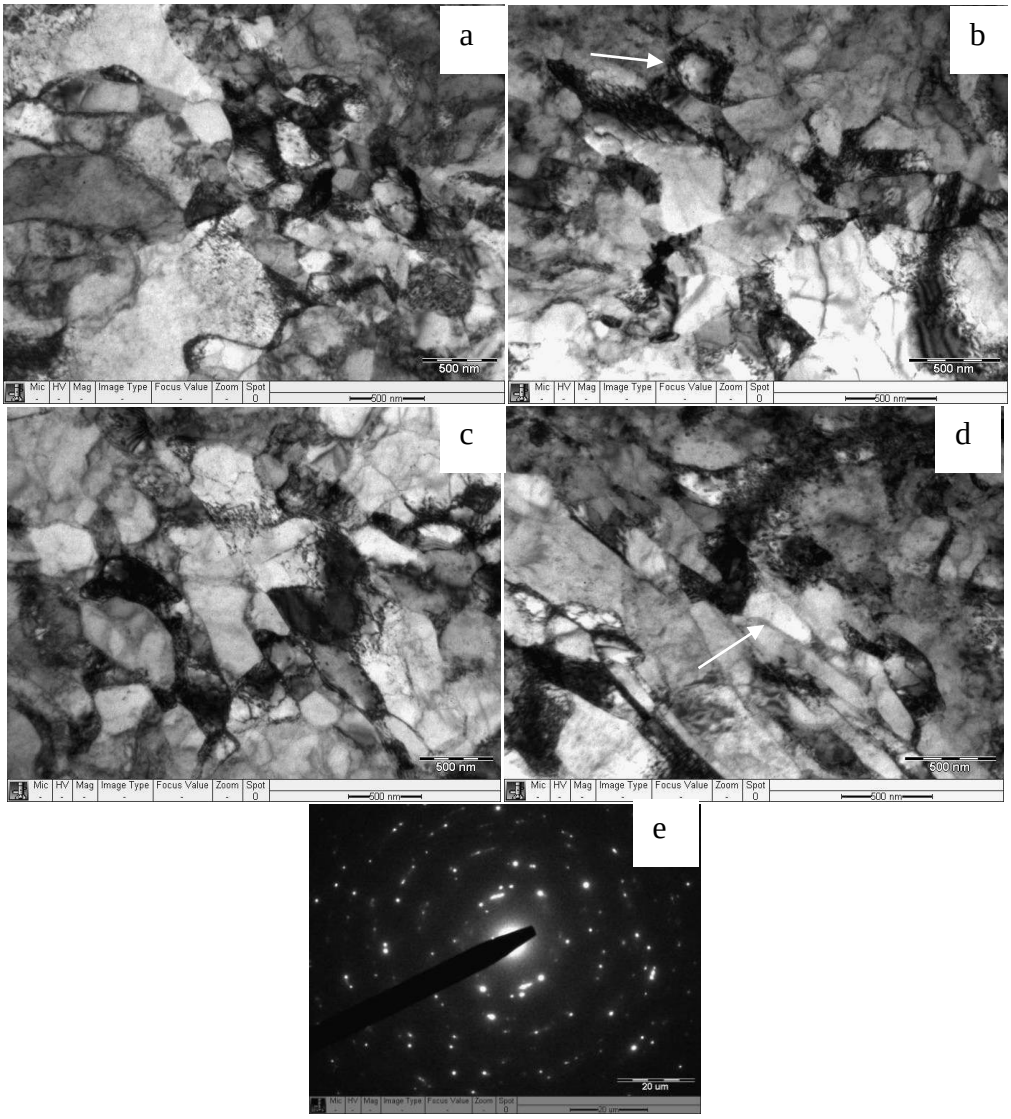


***Fig. 37. a-d)*** *Transmission electron microscopy images of the solution treated ECAP 110º Cu-0.6Cr-0.08Zr alloy,* ***e)*** *selected area electron diffraction pattern.*

# EBSD Data

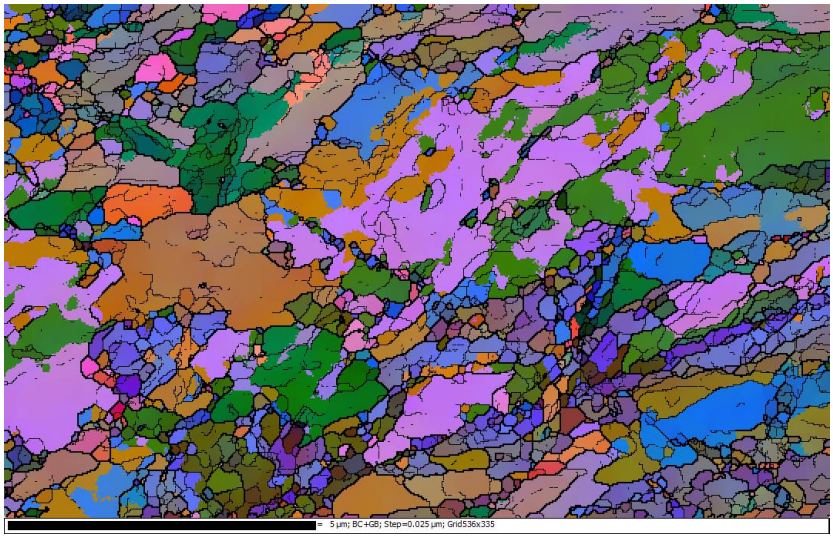

*Fig. 38. Typical EBSD map from EBSD analysis of the alloy processed with die having-Φ=110°-(Euler+grain boundaries).*

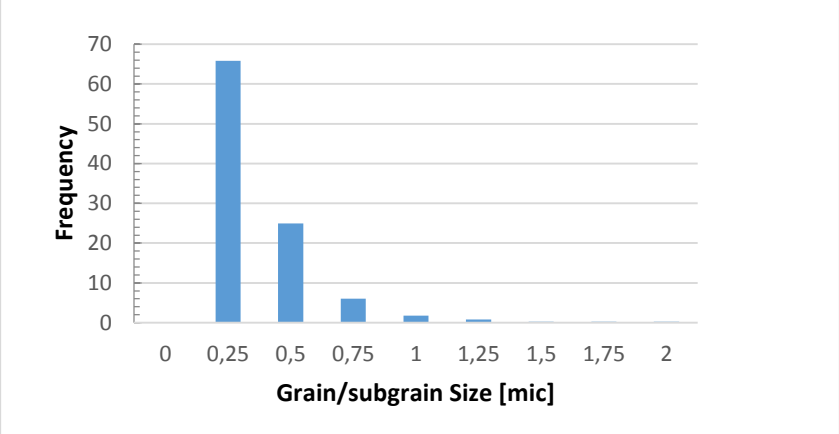


*Fig. 39. Histogram of grain/subgrain size distribution in the alloy processed with die having an angle Φ =110°.*

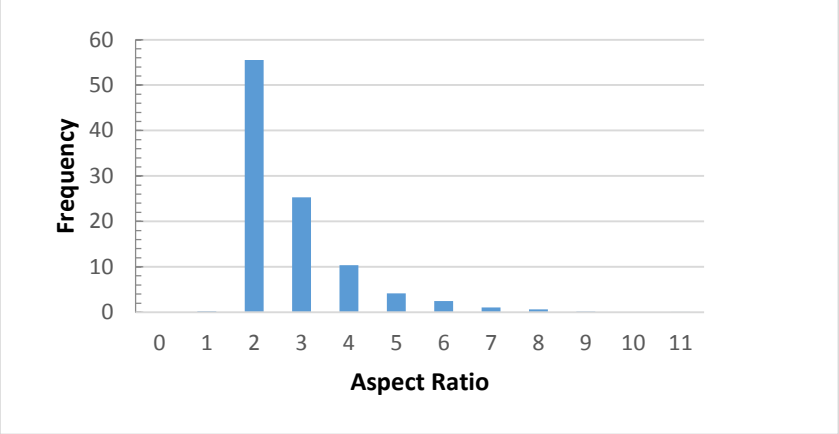


*Fig. 40. Histogram of aspect ratio distribution of grains/subgrains in the alloy processed with die having an angle Φ =110°.*

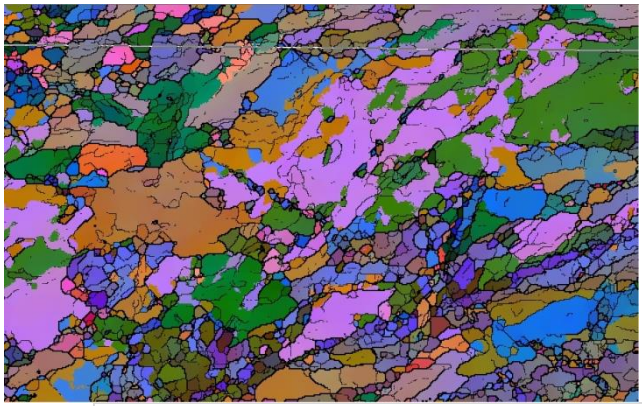

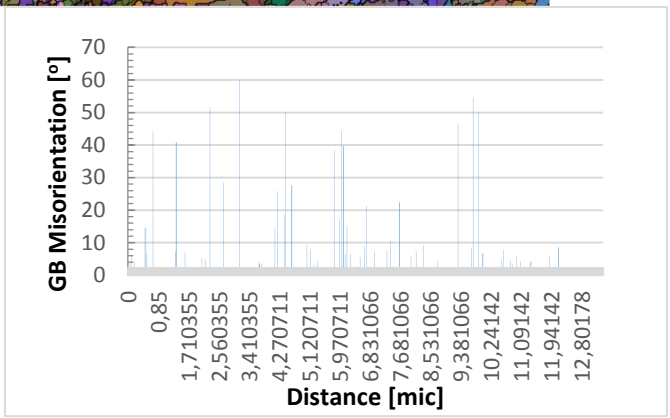
GB Misorientation [°]
70
60
50
40
30
20
10
0
0
0,85
1,710355
2,560355
3,410355
4,270711
5,120711
5,970711
6,831066
7,681066
8,531066
9,381066
10,24142
11,09142
11,94142
12,80178
Distance [mic]

*Fig. 41. Profile through the EBSD map (left) and misorientation of grain/subgrain boundaries along the profile.*

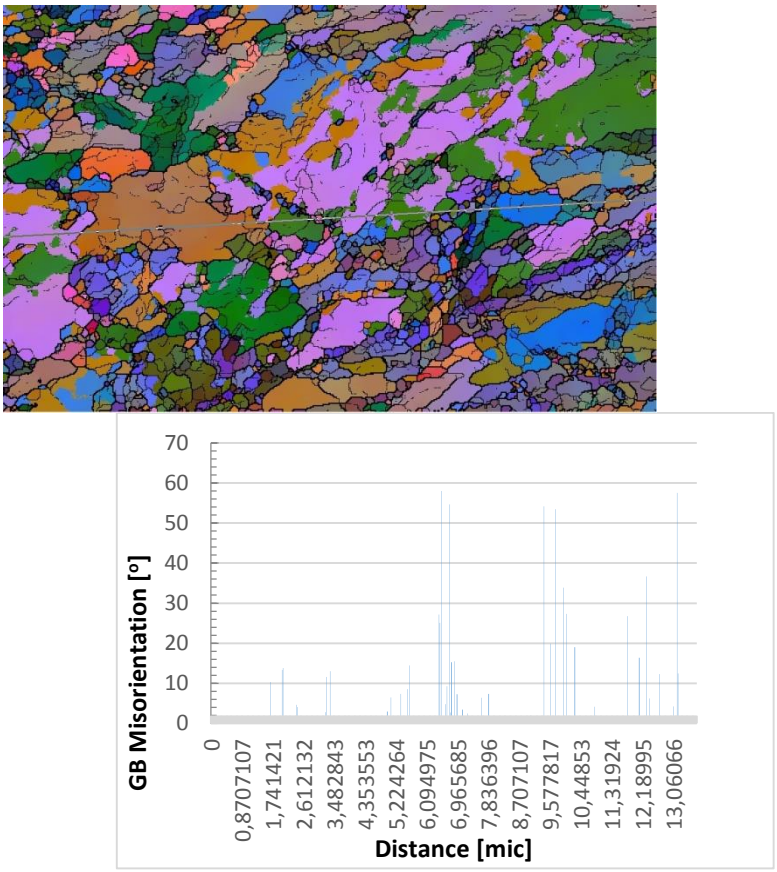


*Fig. 42. Profile through the EBSD map (left) and misorientation of grain/subgrain boundaries along the profile.*

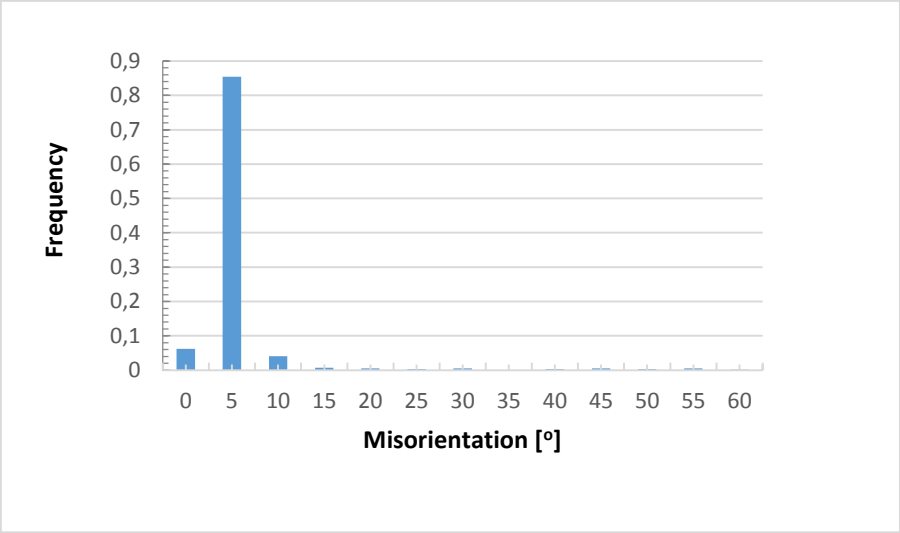


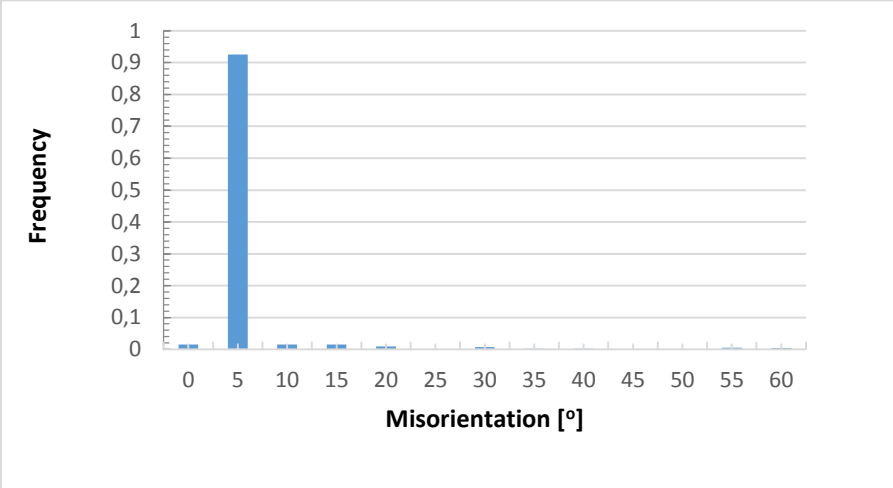


*Fig. 43. Histogram of grain boundary misorientation from the profiles in Fig. 41 and 42.*

### 4.1.3. Microstructure after ECAP 90º

Transmission electron microscopy images of the microstructure of the Cu-0.6Cr-0.08Zr alloy after ECAP processing with a die having Φ =90º for 8 passes are presented in Fig.

44. Qualitative analysis of the TEM images shows that microstructure consists of ultra-fine grains and subgrains having a size below 400 nm (marked by white arrows), though the fraction of subgrains is lower compared to the previous condition No cells are seen in the microstructure (Fig. 44b). Most of grain/subgrain boundaries is well defined.

Figure 45 illustrates typical EBSD map for the Cu-0.6Cr-0.08Zr alloy after ECAP processing with a die having $\Phi = 90^{o}$ for 8 passes in the Y plane (Fig. 1). The outcomes of analysis of EBSD map are in a very good accordance with the TEM observations. Majority of structural elements (such as grains or subgrains) have a size below 0.4 μm (Fig. 46). Profiles passed through the EBSD map clearly show that majority of grain boundaries have high angle misorientation (Fig. 48 and 49), that is also clearly indicated in the histograms of distribution of grain boundary misorientation presented in Fig 50.

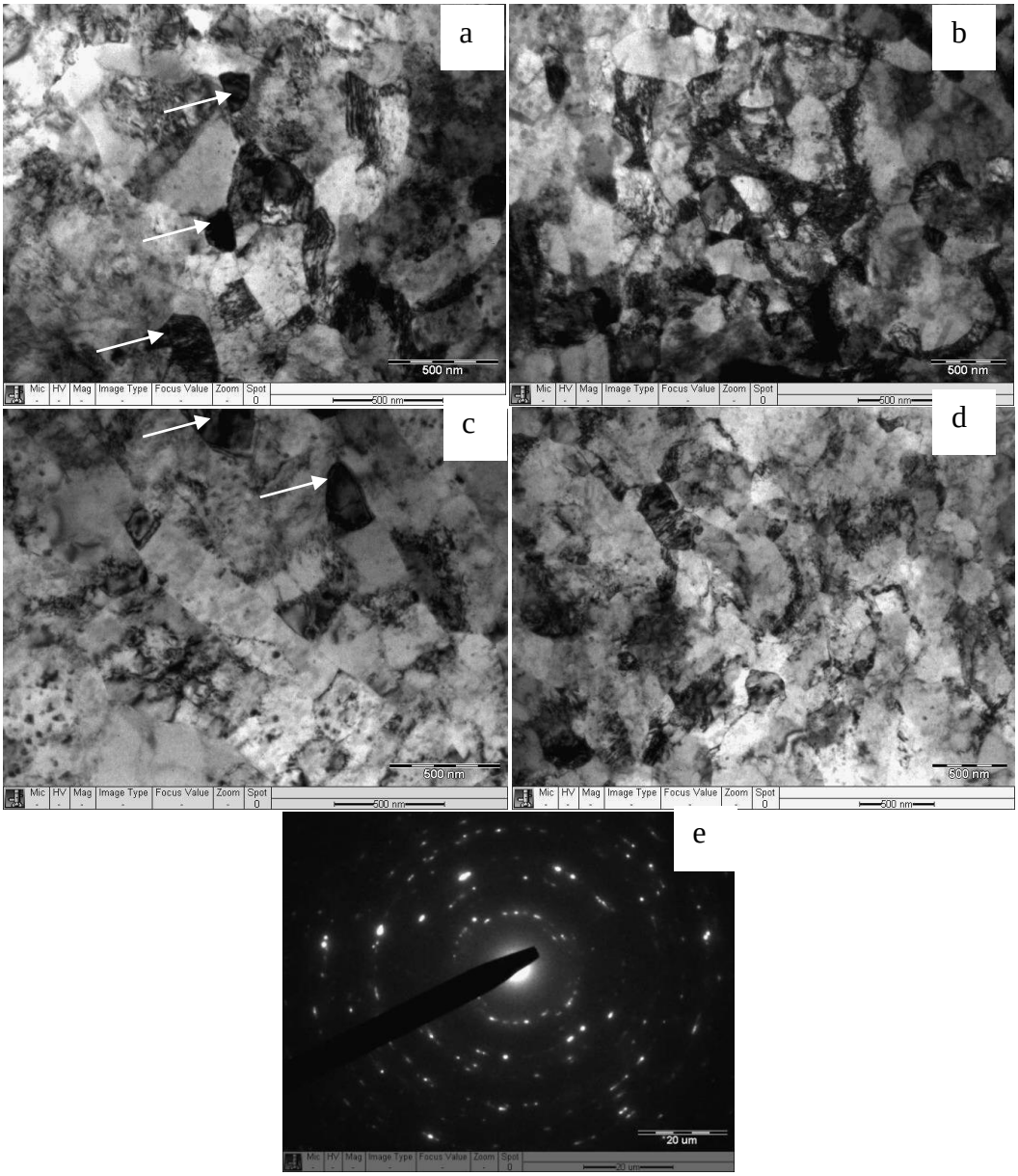


***Fig. 44. a-d)*** *Transmission electron microscopy images of the solution treated ECAP 90º Cu-0.6Cr-0.08Zr alloy;* ***e)*** *selected area electron diffraction pattern.*

# EBSD Data

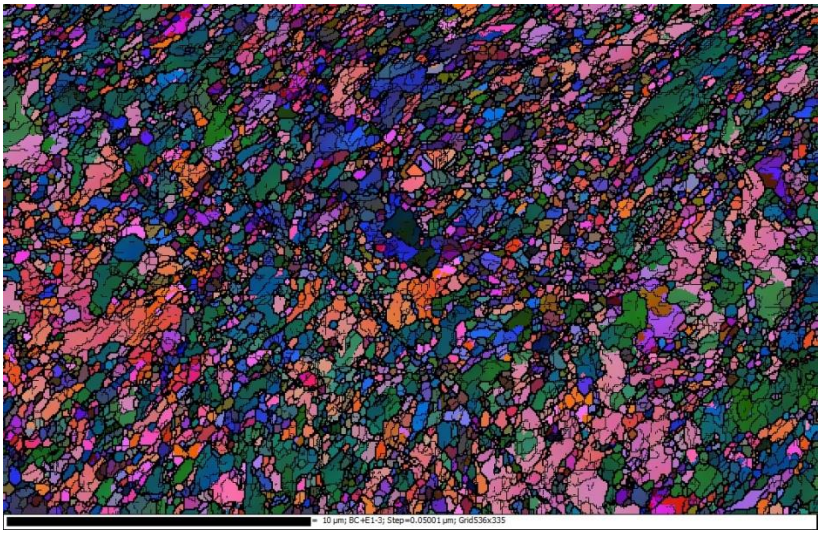

*Fig. 45. Typical EBSD map from EBSD analysis of the alloy processed with die having-Φ=90°-(Euler+grain boundaries).*

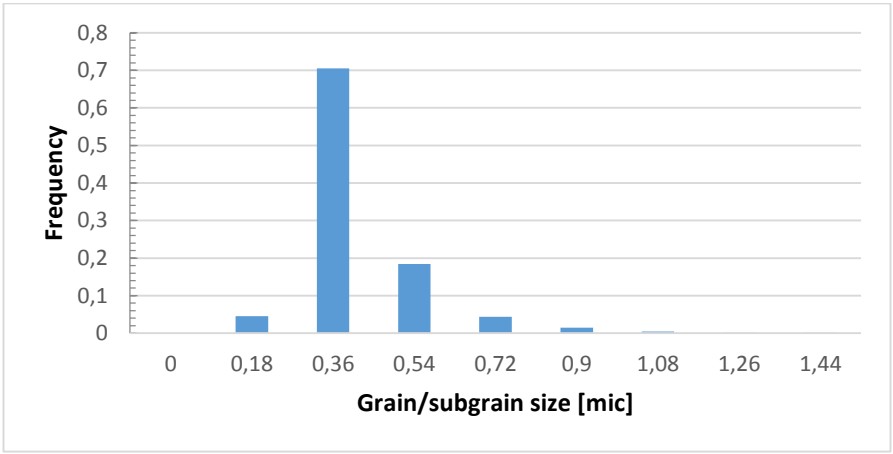


*Fig. 46. Histogram of grain/subgrain size distribution in the alloy processed with die having an angle Φ =90°.*

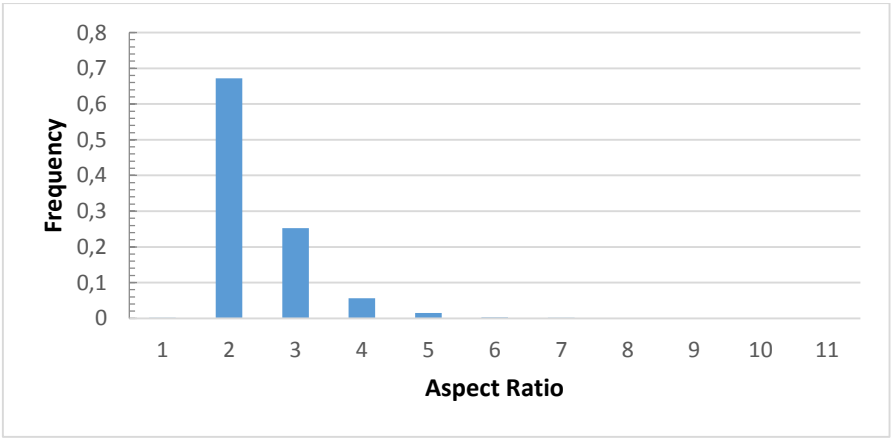


*Fig. 47. Histogram of aspect ratio distribution of grain/subgrain in the alloy processed with die having an angle Φ =90°.*

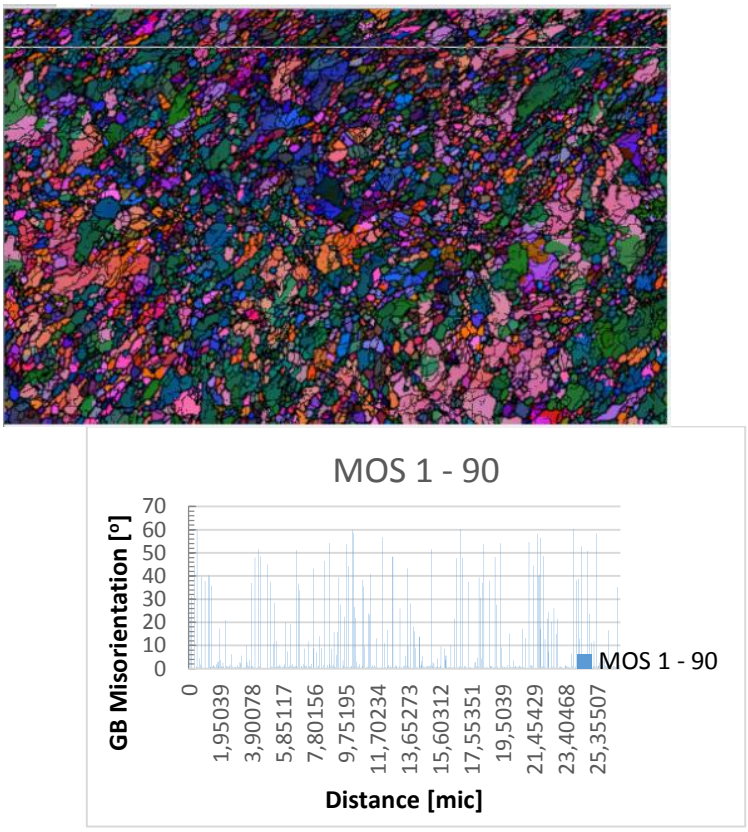


*Fig. 48. Profile through the EBSD map (left) and misorientation of grain/subgrain boundaries along the profile.*

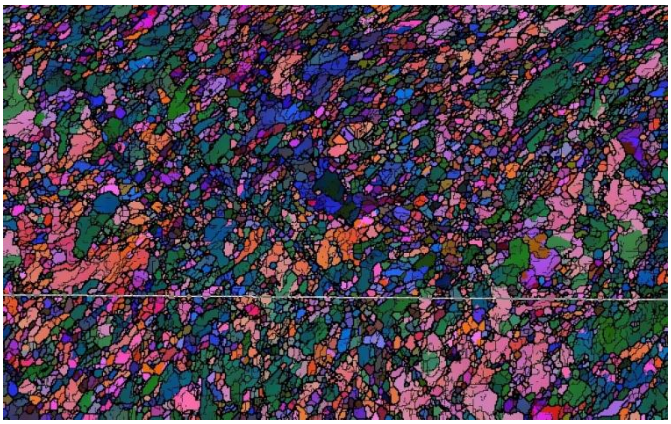

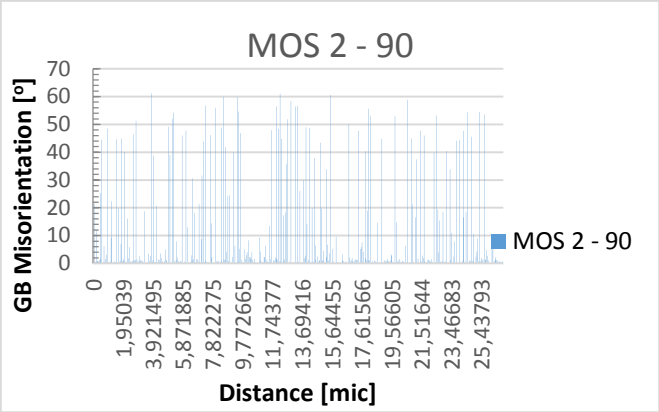


*Fig. 49. Profile through the EBSD map (left) and misorientation of grain/subgrain boundaries along the profile.*

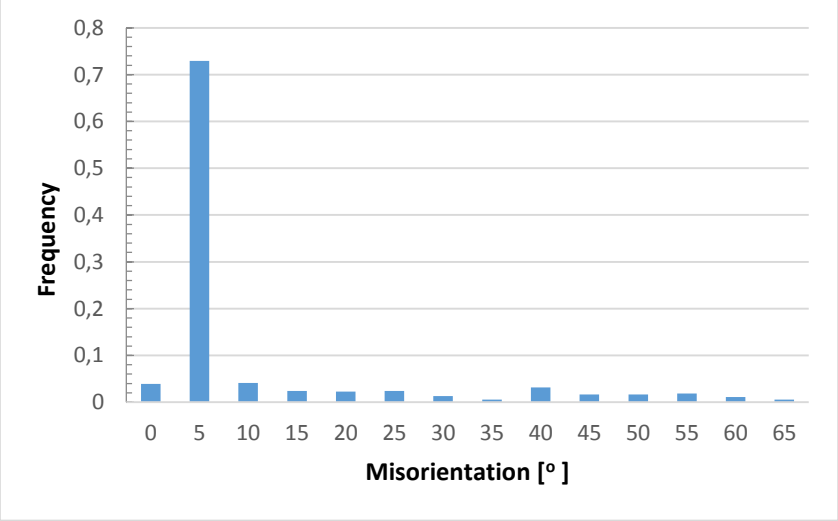

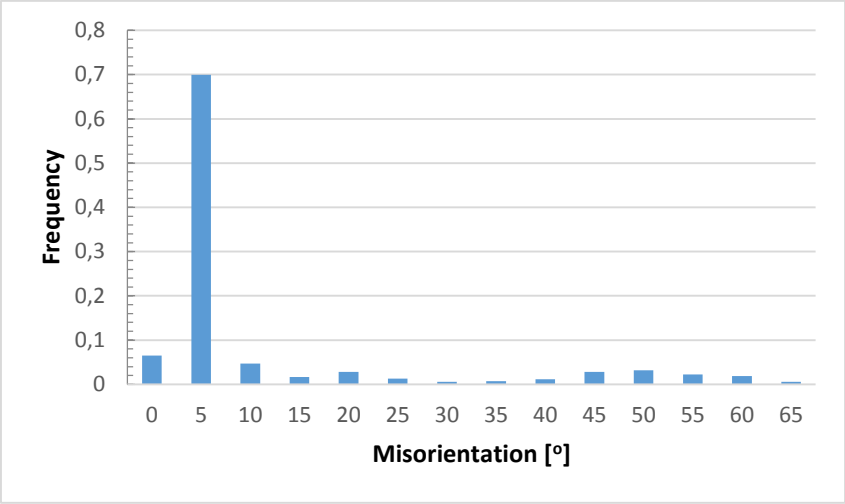


*Fig. 50. Histograms of grain boundary misorientation from the profiles in Fig. 48 and 49.*

## 4.2. Effect of ECAP processing on uni-axial tensile properties

Typical engineering stress-strain curves from uni-axial tensile testing of the Cu-0,6Cr-0.08Zr alloy are presented in Figs. 51-55. These curves were carefully analyzed as described in Section 3.31, and the data on 0.2% proof strength, ultimate tensile strength, uniform elongation and elongation to failure were determined. These data are listed in Table 2. It is clearly seen from curves on Figs. 51-55 and Table 2, that grain refinement dramatically affects mechanical behaviour and properties of Cu-0.6Cr-0.08Zr alloy. After ECAP processing, the 0.2% proof strength increases by a factor of ~4, whereas ultimate tensile strength of the material is nearly doubled. However, the ductility of the material (uniform elongation and elongation to failure) is dramatically reduced. It should be noted that mechanical behaviour of the ECAP processed materials strongly depends on the ECAP processing route applied to the material. Particularly, more intensive grain refinement in the alloy after ECAP processing with die having SYMBOL=90$^{o}$ results in higher mechanical strength due to finer grains achieved in the material (see Sections 4.1.2 and 4.1.3 above). Higher fraction of high angle grain boundaries also leads to better uniform elongation in the ECAP processed material with die having an angle of 90$^{o}$ (see Sections 3.1.2 and 3.1.3). As is well known, both grain size and fraction of high angle grain boundaries have a significant effect on mechanical properties of UFG metallic materials [86]. Grain boundaries are effective obstacles for the movement of dislocations, so dislocations pile up at grain boundaries. Pile-ups in finer grains contain fewer dislocations, the stress at the tip of the pile-up decreases and, thus, a larger stress is required to cause slip in the adjacent grain, resulting in increase of yield strength with decreasing grain size according to the well-known Hall-Petch law [28, 29]. High angle grain boundaries are more effective from the viewpoint of strengthening of the metallic materials [87].

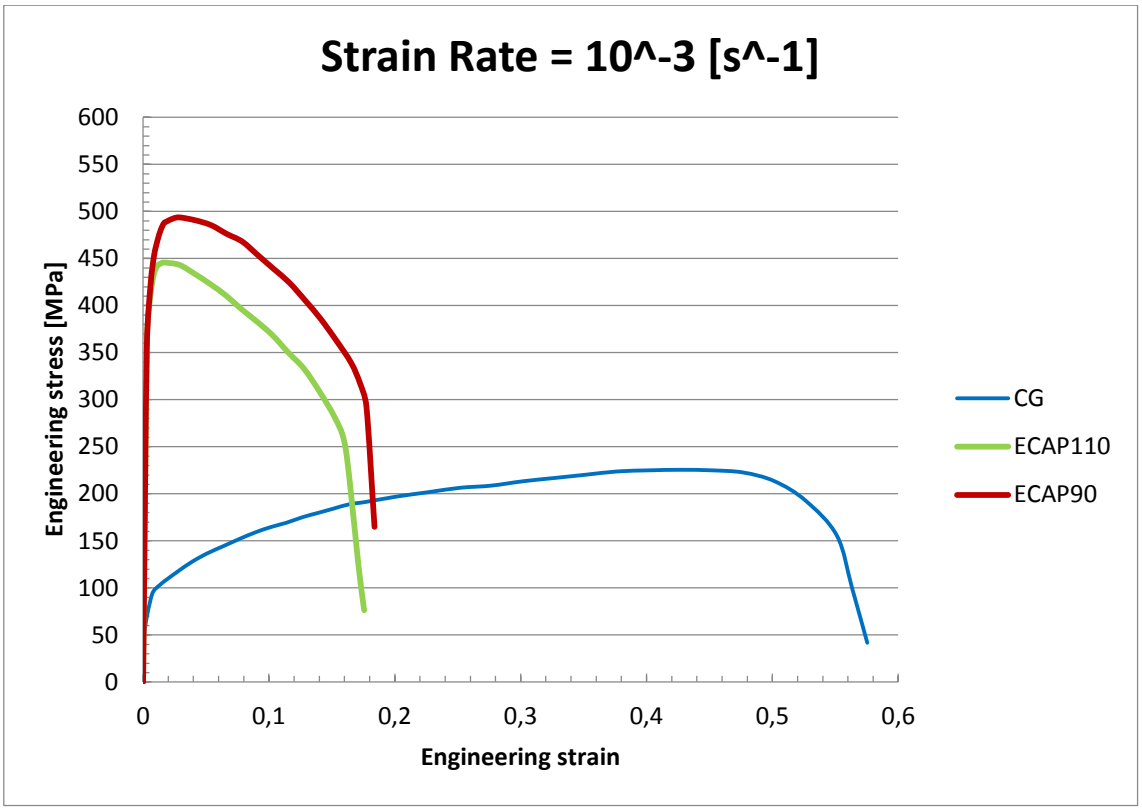


*Fig. 51. Engineering stress - strain curves from uni-axial tensile testing of the Cu-0.6Cr-0.08Zr alloy at room temperature with strain rate of = $10^{-3}$ $s^{-1}$.*

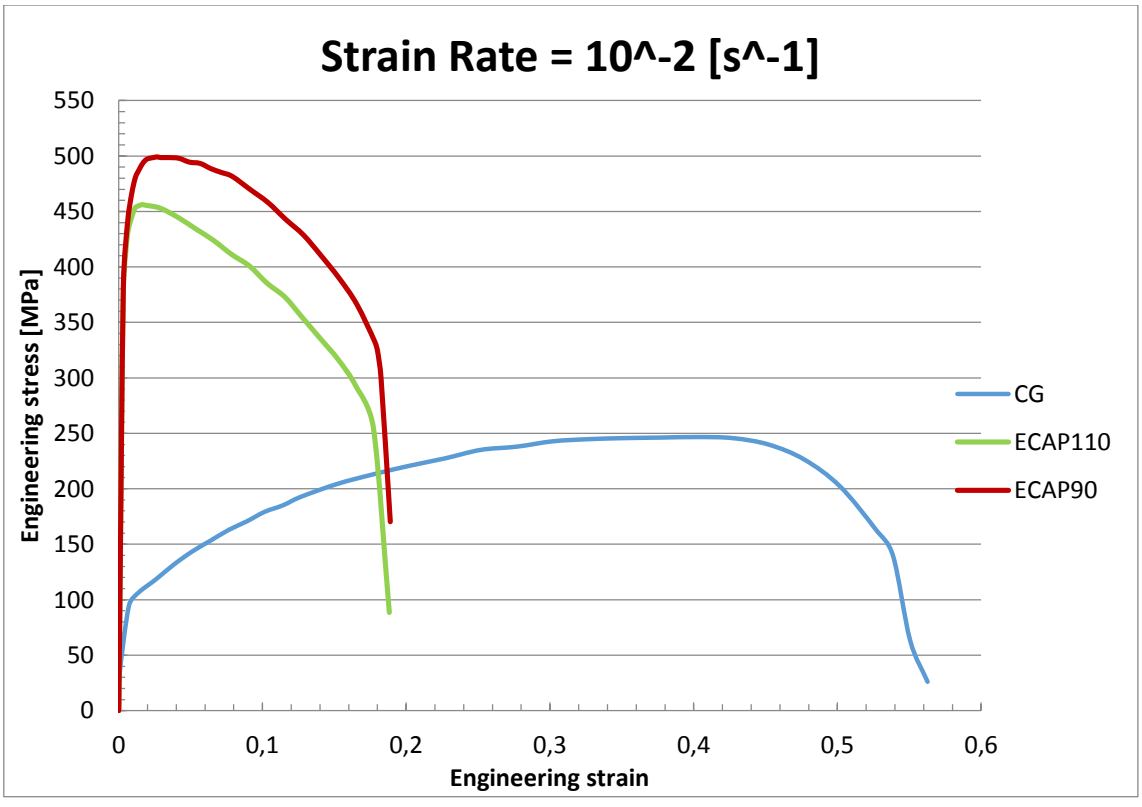


*Fig. 52. Engineering stress - strain curves from uni-axial tensile testing of the Cu-0.6Cr-0.08Zr alloy at room temperature with strain rate of = $10^{-2}$ $s^{-1}$.*

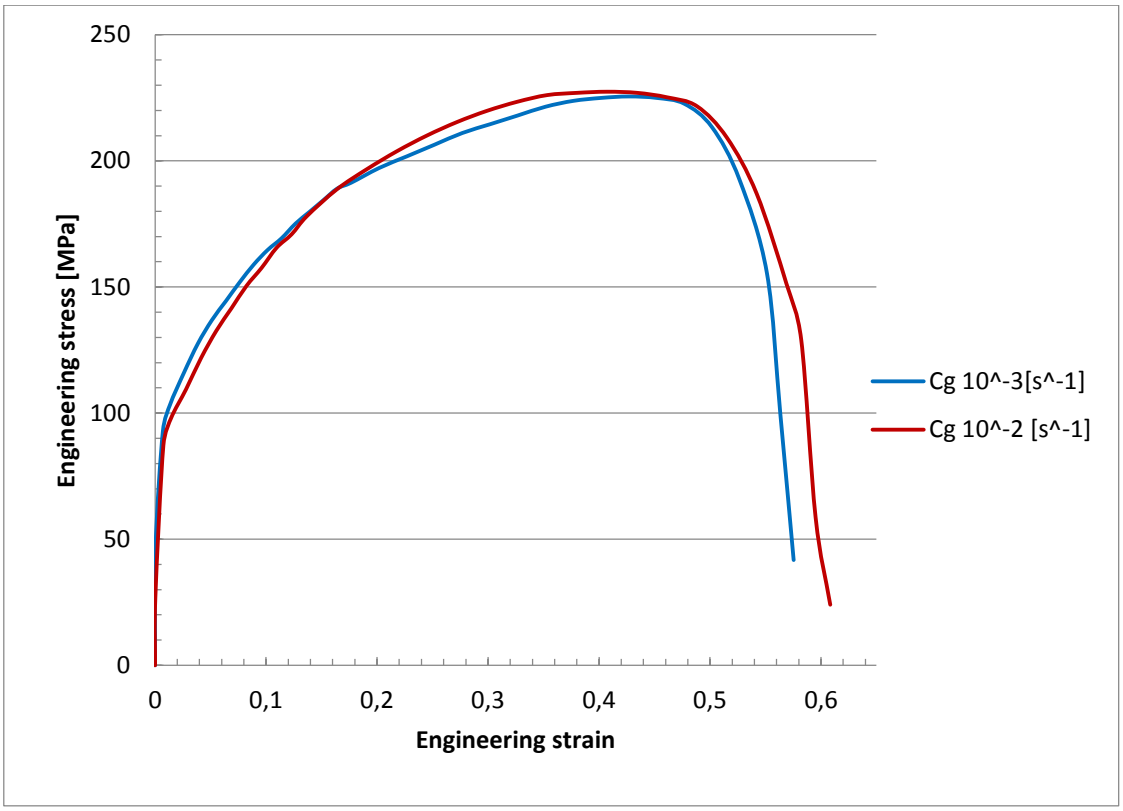


*Fig. 53. Engineering stress - strain curves from uni-axial tensile testing of the CG Cu-0.6Cr-0.08Zr alloy at room temperature.*

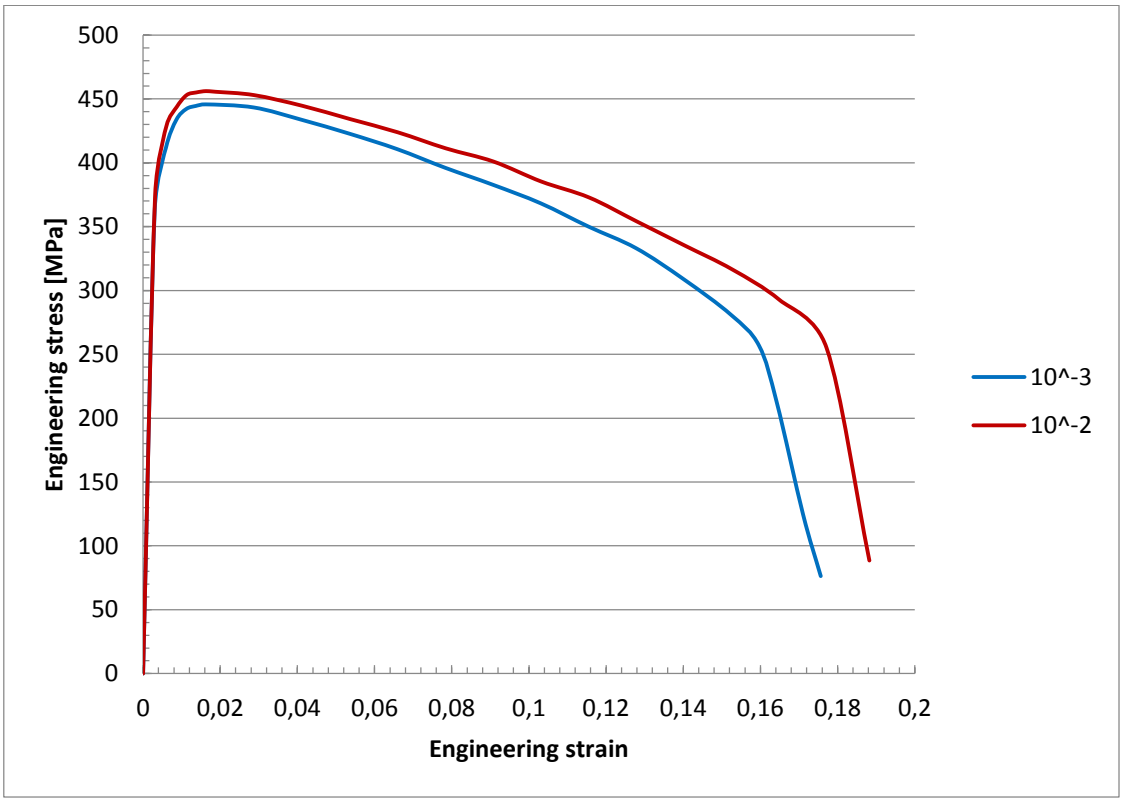


*Fig. 54. Engineering stress - strain curves from uni-axial tensile testing of the ECAP 110$^{o}$ Cu-0.6Cr-0.08Zr alloy at room temperature.*

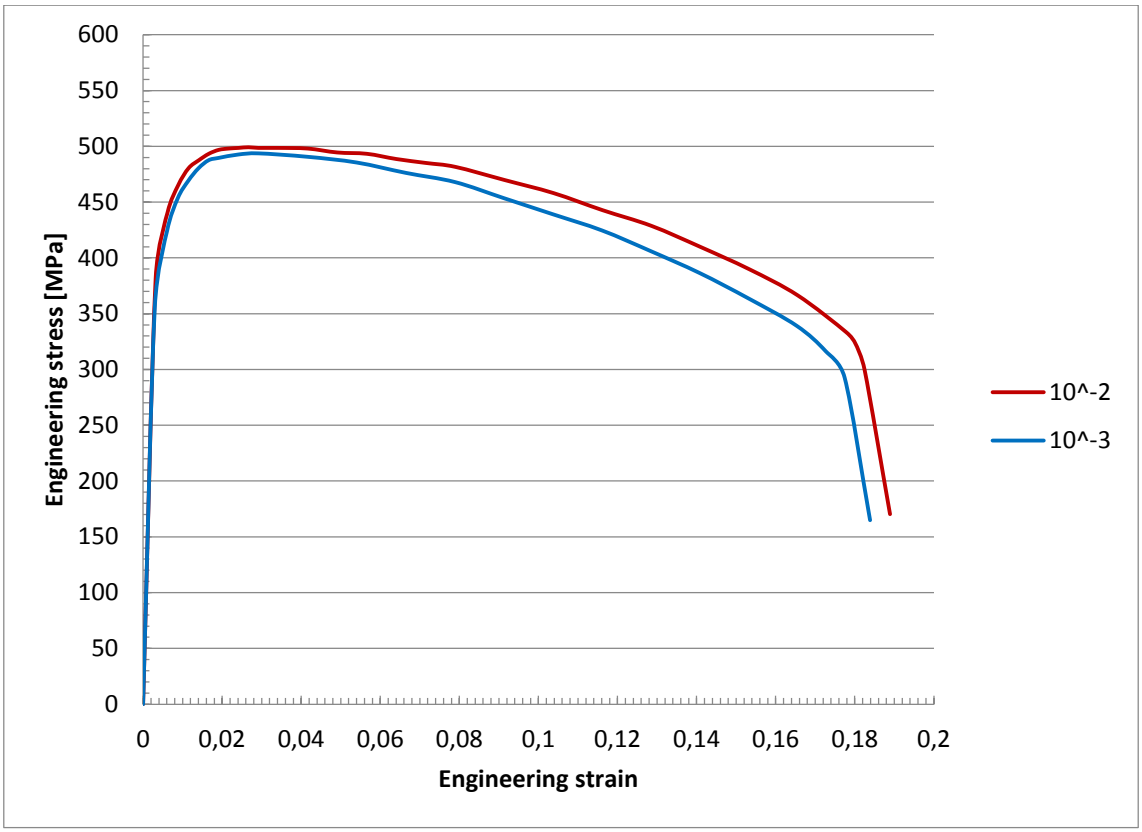


*Fig. 55. Engineering stress - strain curves from uni-axial tensile testing of the ECAP 90º Cu-0.6Cr-0.08Zr alloy at room temperature.*

Table 2. Data on mechanical properties of the Cu-0.6Cr-0.08Zr alloy before and after ECAP processing.

| Material | Strain rate [$s^{-1}$] | $\sigma_{0,2}$ [MPa] | $\sigma_{UTS}$[MPa] | $\varepsilon_u$ (%) | $\varepsilon_f$ (%) |
|---|---|---|---|---|---|
| CG | $10^{-3}$ | 82 | 226 | 42,7 | 54,6 |
| | $10^{-2}$ | 89 | 227 | 38,0 | 57,4 |
| ECAP 110º | $10^{-3}$ | 404 | 446 | 1,6 | 15,9 |
| | $10^{-2}$ | 420 | 456 | 1,6 | 17,3 |
| ECAP 90º | $10^{-3}$ | 410 | 494 | 2,9 | 16,3 |
| | $10^{-2}$ | 431 | 499 | 2,6 | 17,7 |

Figure 56 illustrates engineering stress - strain curves from strain rate jump tests. The data on strain rate sensitivity calculated according to Eq. 16 are presented in Table 3. It is seen that ECAP processed materials show higher strain rate sensitivity by a factor of 3 compared to the coarse-grained one. This can be related to UFG microstructure formed in the ECAP processed materials, which is known to increase strain rate sensitivity of the face centered cubic (fcc) metals and alloys [3].

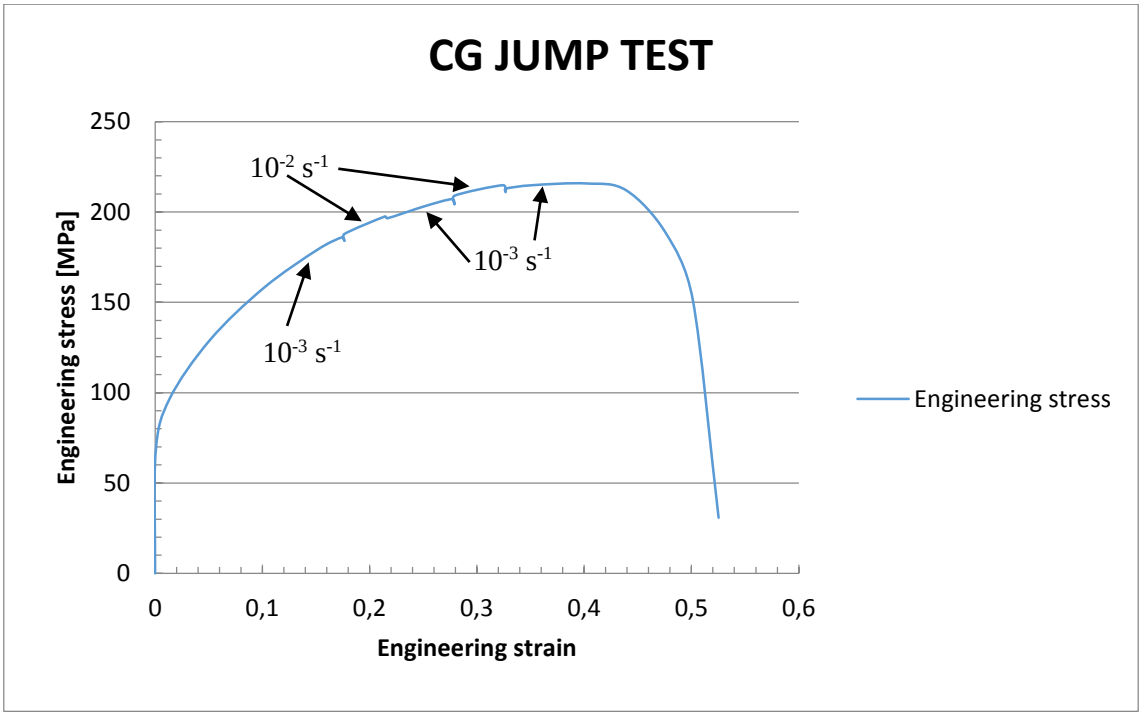


*Fig. 56. Tensile strain rate jump test from strain rate $10^{-3}$ $s^{-1}$ to strain rate $10^{-2}$ $s^{-1}$ on the CG alloy.*

Table 3. Data on strain rate sensitivity.

| Material | Strain rate sensitivity |
|---|---|
| Coarse Grained | 0.011 |
| ECAP 110º | 0.031 |
| ECAP 90º | 0.032 |

## 4.3. Bi-axial stretching formability of Cu-0.8Cr-0.06Zr alloy before and after ECAP processing.

This section focuses on results of small punch testing of the Cu-0.6Cr-0.08Zr alloy in different conditions. Figure 34 illustrates typical load-central deflection curves from small punch testing of the material. The curves are plotted in that way, so the effect of ECAP processing and punch speed on mechanical behavior can be clearly seen. On all curves, four typical stages of deformation (see Section 3.3.2) can be easily identified. Elastic bending of samples is followed by plastic bending, which, in turn, is followed by membrane (bi-axial) stretching and finally by cracking and failure of specimens. It should be noted that the test was stopped before onset of the final stage (cracking and failure), so the last stage cannot be seen in most of the curves. From these curves, data on maximum load reached in the material and maximum central deflection before onset of cracking were determined and listed in Table 4.

The analysis of load-central deflection curves from small punch testing clearly shows that grain refinement results in higher load (or in higher stress) required to deform the material in biaxial stretching mode (Figs. 57-62, Table 4), similar to the case of uni-axial tensile testing (see Section 4.2). However, there is no any significant reduction of maximum central deflection in the samples after ECAP processing, which indicates that their ductility (formability) in bi-axial stretching mode was not reduced. Particularly, the $h_{max}$-value in the specimens tested with punch speed of 0.05 mm/min was reduced from 1.47 mm for coarse-grained material to 1.37 and 1.33 mm for the material after ECAP processing with dies having $110^o$ and $90^o$, respectively. The reduction of the $h_{max}$-values in samples after ECAP processing is more pronounced at higher punch speeds, but still remains insignificant. In order to quantify the ductility (or formability) of the material in the bi-axial stretching mode, each tested specimen having a shape of dome was sectioned in two halves, so one could measure thickness of the area deformed in biaxial stretching, to compare it with the initial thickness of the samples and, thus, to determine the plastic strain which can be induced into material by bi-axial stretching without any cracking. The typical cross-sections of two specimens are presented in Fig. 66-67. The area of bi-axial stretching can be easily identified (it is marked by white circles). Data on true strain induced into samples by bi-axial stretching are summarized in Table 5. It is seen that grain refinement did not lead to significant reduction of formability of the material. Strain rate effect on the biaxial stretching formability of the material can be also noted. The alloy after ECAP processing via both processing routes shows higher biaxial stretching formability at the highest punch speed of 5 mm/min. This can be related to suppression of dislocation annihilation mechanisms during plastic deformation of the UFG alloys, resulting in their accumulation in the interior of ultra-fine grains/subgrains, which provides their enhanced strain hardening ability and delays localization of plastic deformation at the macro scale, i.e. necking [3].

From the results of small punch testing, it is seen that there is nearly no effect of punch speed (or strain rate) on the load (or stress) during biaxial stretching of the coarse-grained alloy (Fig. 60). However, the effect of punch speed on the load required for deformation of ECAP processed materials can be noted. It is seen from Figs. 61 and 62, that load

(stress) required for biaxial stretching of the ECAP processed materials increases with increasing punch speed (strain rate). To measure strain rate sensitivity during bi-axial stretching, punch speed jump tests were carried out. The punch speed was rapidly changed from 0.05 mm/min to 0.5 mm/min during bi-axial stretching of the specimens in all studied conditions. The load-central deflections curves from punch speed jump tests are presented in Figs. 63-65. Similar to the case of strain rate jump tests, the strain rate sensitivity was measured as

$$m = \frac{\partial \ln(F)}{\partial \ln(v)} \equiv \frac{\ln(F_2 / F_1)}{\ln(v_2 / v_1)} \quad (17)$$

where $F_2$ and $F_1$ are the values of the load corresponding to the punch speeds of $v_2$ and $v_1$, respectively. Back-extrapolation of the load-central deflection curves to the central deflection at which a strain rate jump was made was used to determine the $P_2$ values and the instantaneous strain rate sensitivity. It should be noted that the Eq. 17 should be valid, since the stress during biaxial stretching in small punch testing is proportional to the applied load [88, 89]. Data on strain rate sensitivity of the alloys during small punch testing are summarized in Table 5. It is seen that the ECAP processed alloys tend to demonstrate higher strain rate sensitivity during biaxial stretching compared to the coarse-grained material. However, the strain rate sensitivity values during biaxial stretching (Table 5) are lower compared to those during uni-axial tensile testing (Table 3). This can be related to the change in the deformation mode, which can significantly affect process of dislocation glide in the material and their interaction with each other and obstacles present in the microstructure, such as fine particles, dislocation junctions, grain/subgrain boundaries, etc. The effect of friction between the punch and specimen during small punch testing also cannot be ruled out.

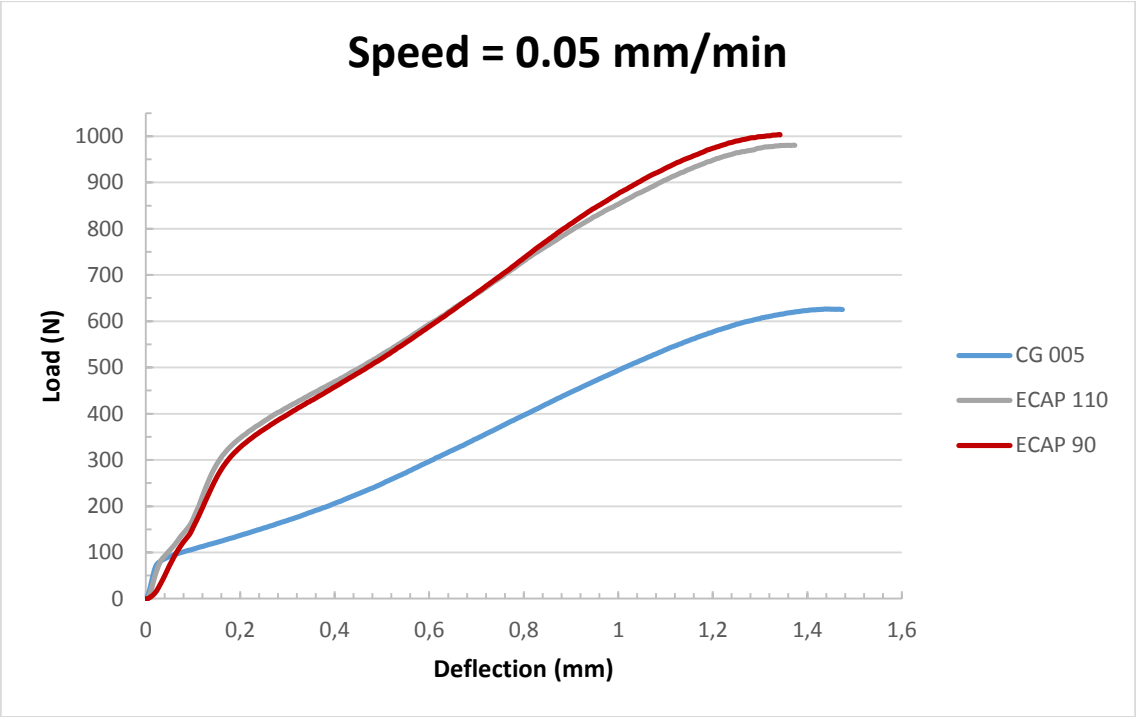


*Fig. 57. Load-central deflection curves from small punch testing of the alloy with punch speed of 0.05 mm/min.*

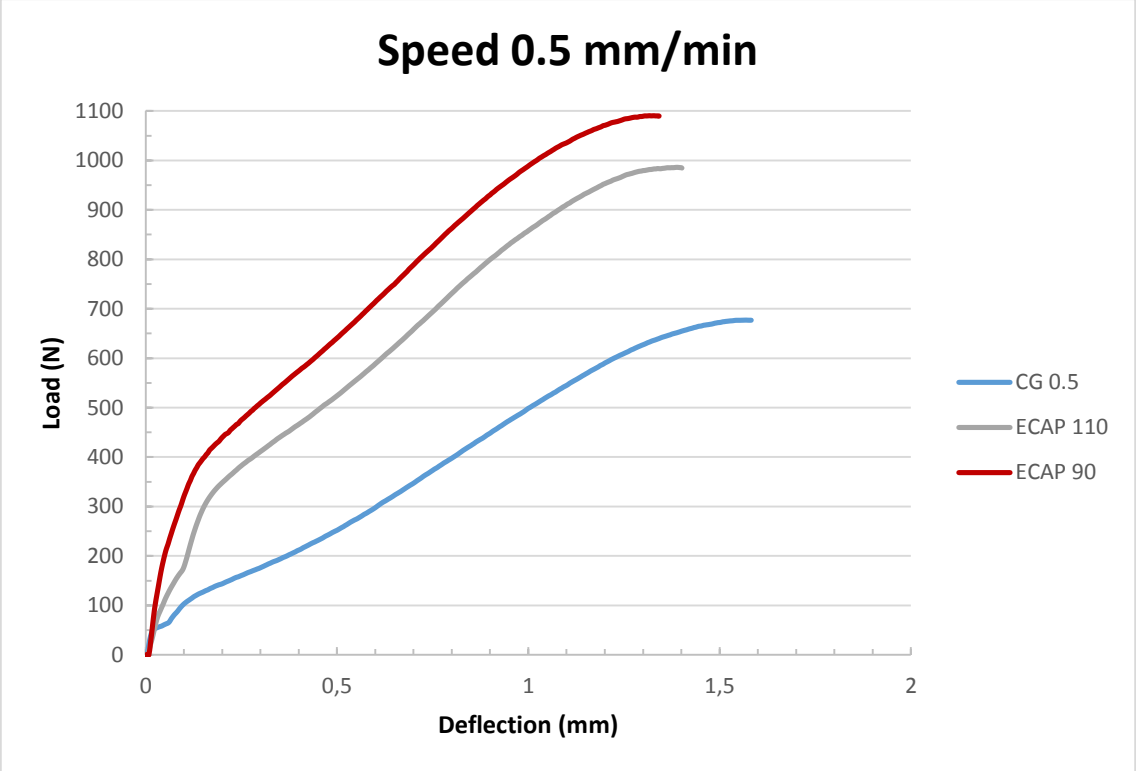


*Fig. 58. Load-central deflection curves from small punch testing of the alloy with punch speed of 0.5 mm/min.*

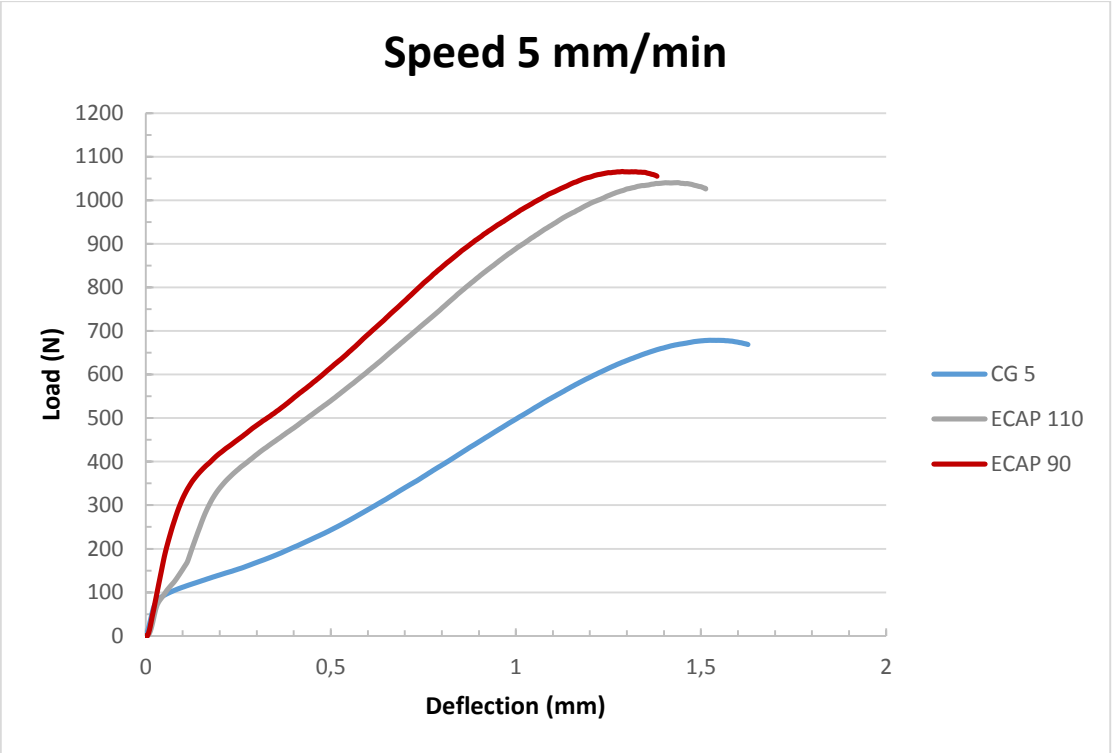


*Fig. 59. Load-central deflection curves from small punch testing of the alloy with punch speed of 5 mm/min.*

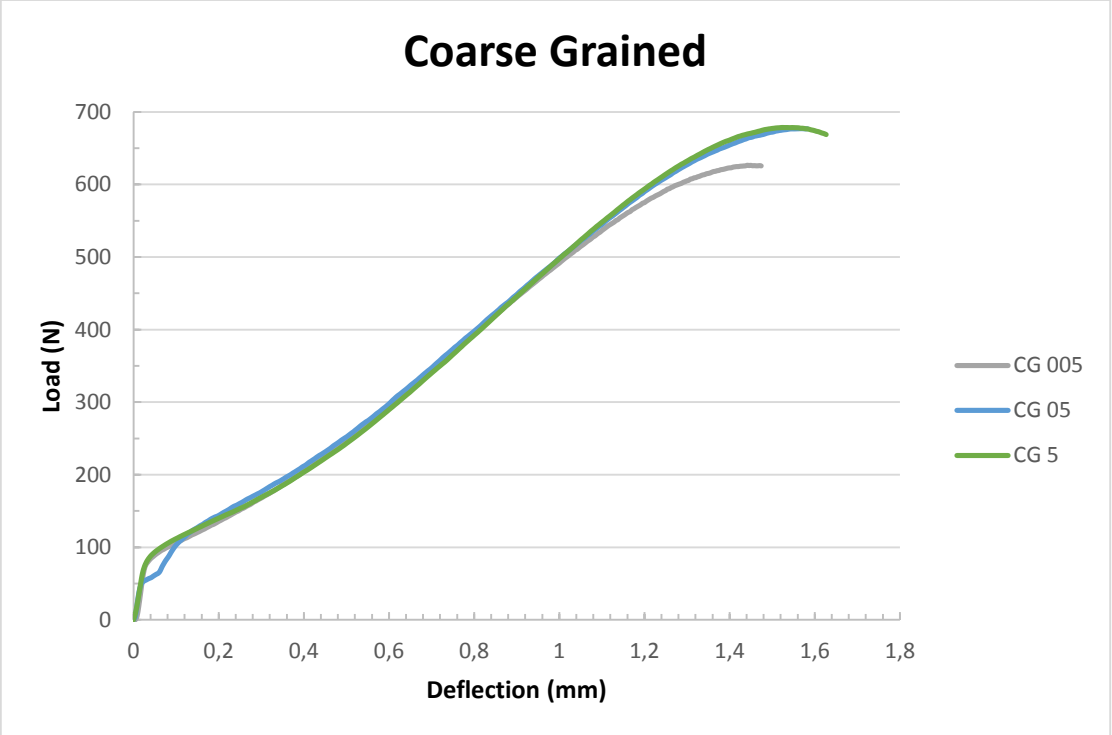


*Fig. 60. Load-central deflection curves from small punch testing of the Coarse Grain (CG) alloy with varying speed of punch.*

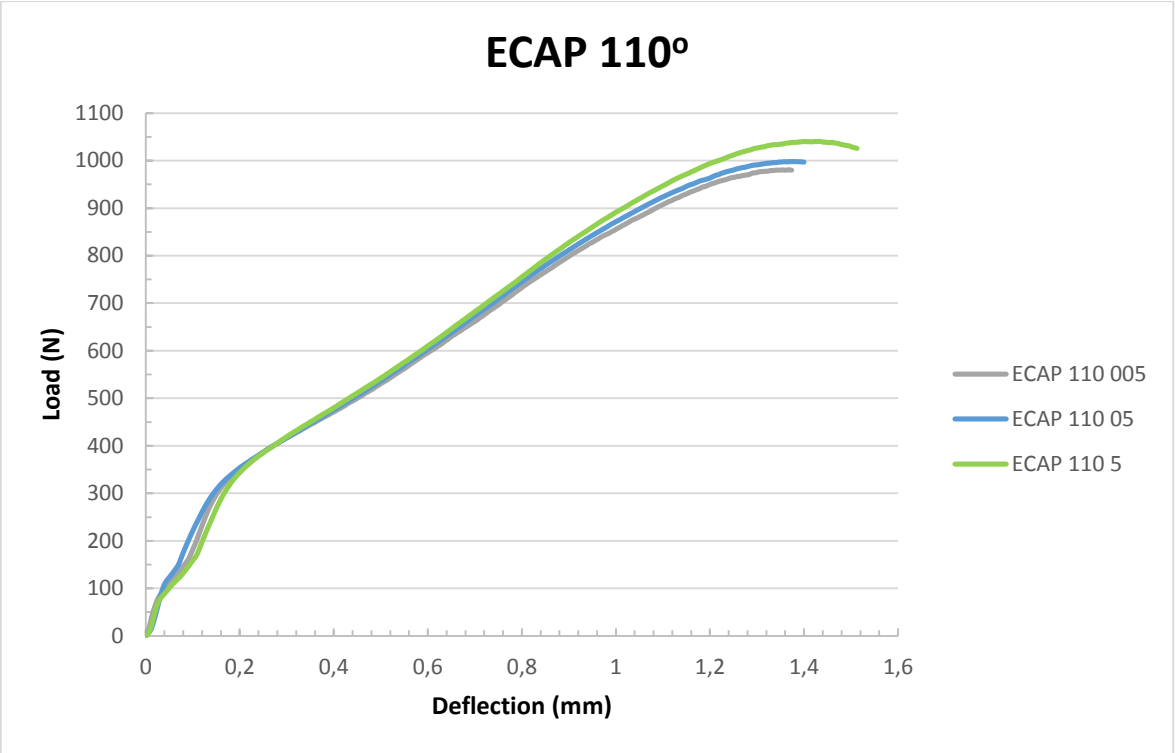


*Fig. 61. Load-central deflection curves from small punch testing of the ECAP 110º alloy with varying speed of punch.*

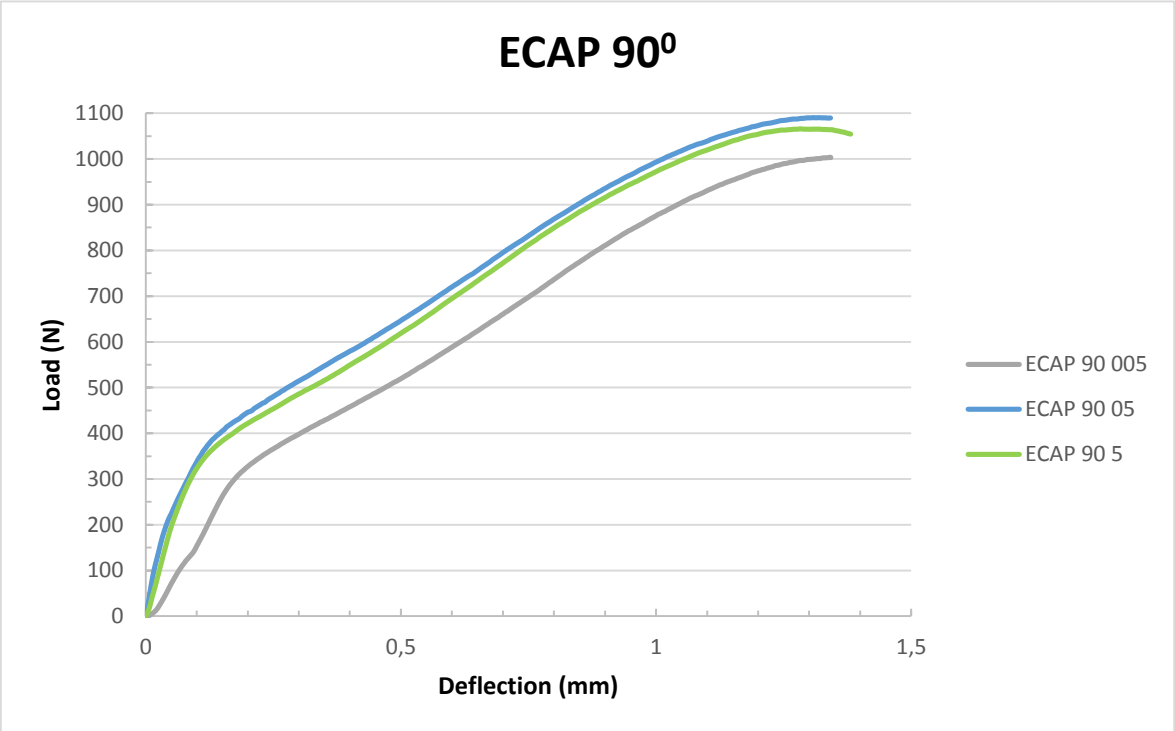


*Fig. 62. Load-central deflection curves from small punch testing of the ECAP 90º alloy with varying speed of punch.*

Table 4. Results from small punch test.

| Material | Speed [mm/min] | $F_{max}$ [N] | $h_{max}$ [mm] |
|---|---|---|---|
| CG | 0,05 | 626 | 1,47 |
| | 0,5 | 678 | 1,57 |
| | 5 | 679 | 1,53 |
| ECAP 110º | 0,05 | 981 | 1,37 |
| | 0,5 | 998 | 1,38 |
| | 5 | 1040 | 1,43 |
| ECAP 90º | 0,05 | 1004 | 1,33 |
| | 0,5 | 1090 | 1,31 |
| | 5 | 1066 | 1,31 |

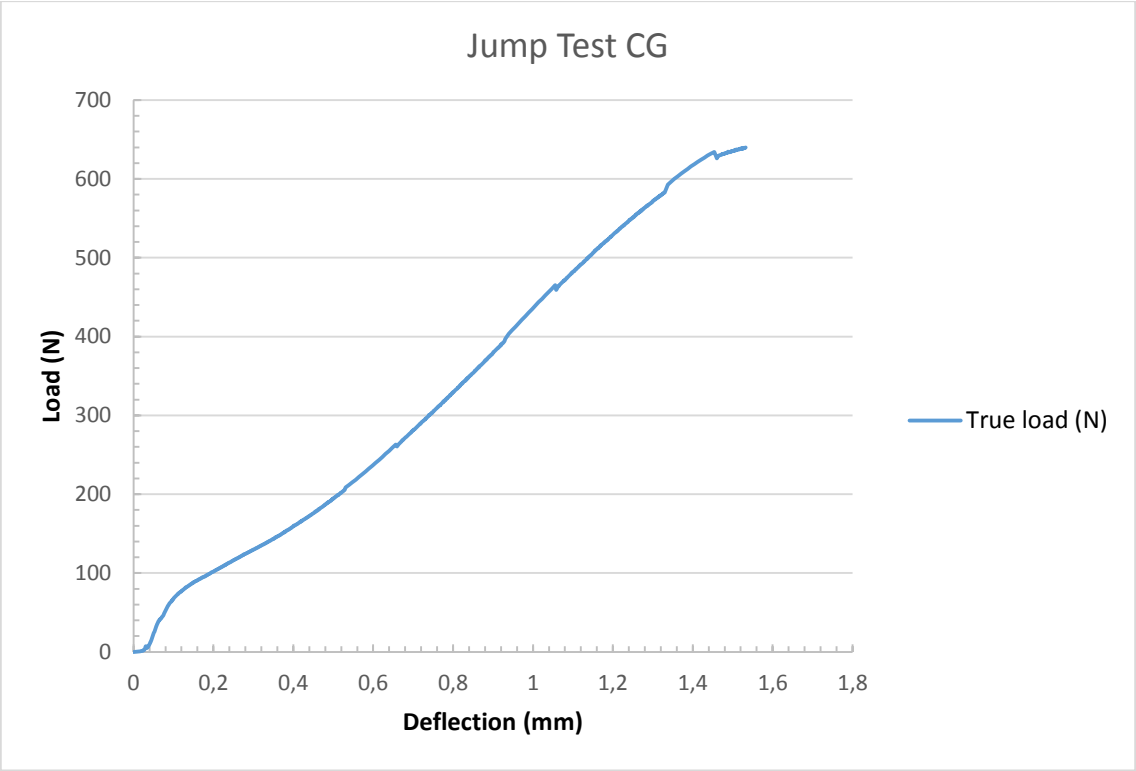


*Fig. 63. Load-central deflection curve from punch speed jump test on the CG alloy.*

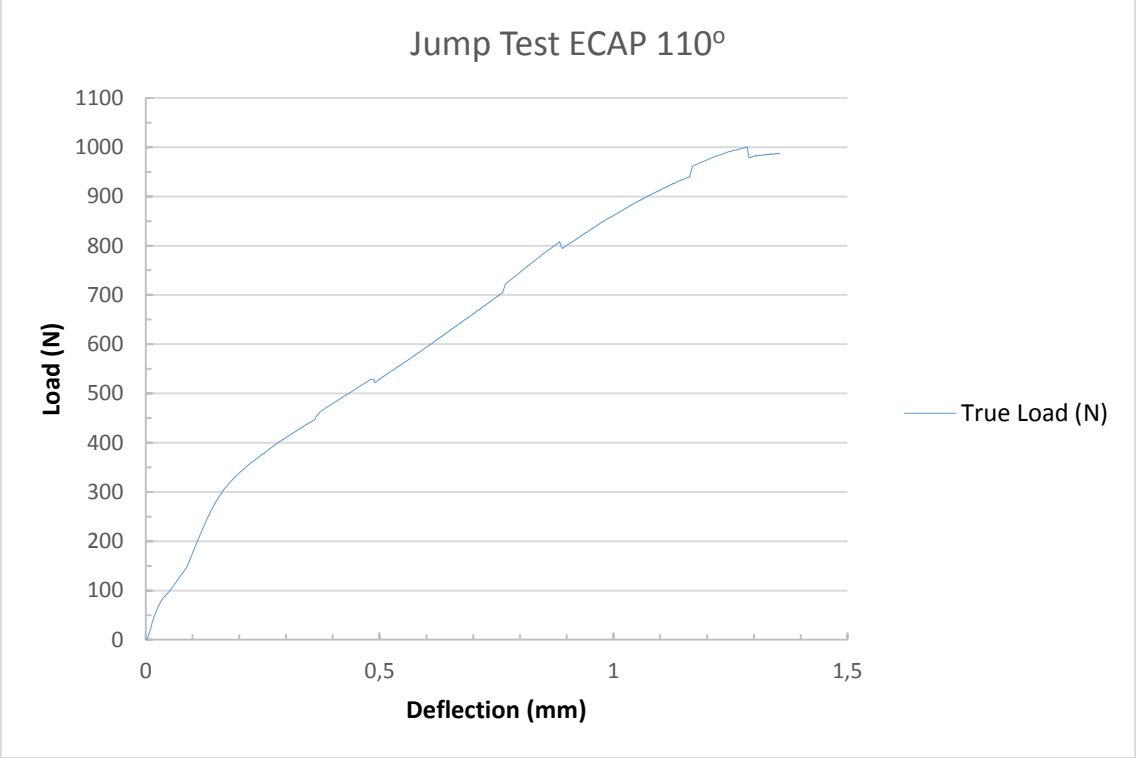


*Fig. 64. Load-central deflection curve from punch speed jump test on the ECAP 110º alloy.*

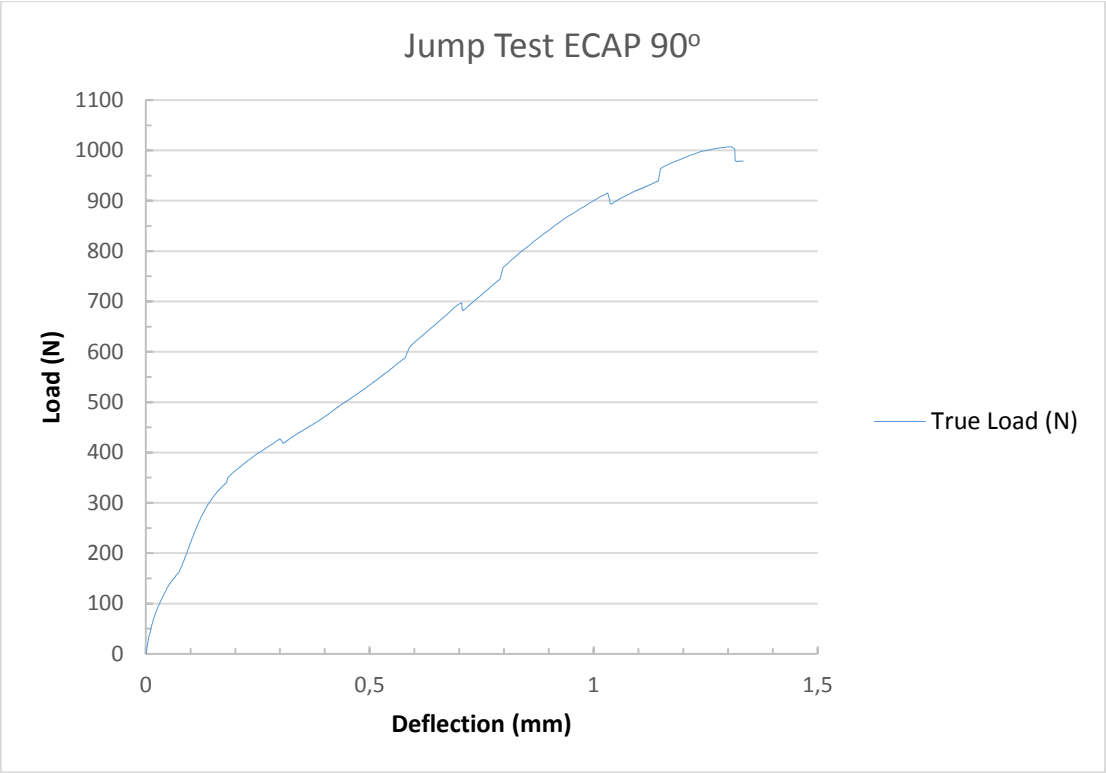


*Fig. 65. Load-central deflection curve from punch speed jump test on the ECAP 90º alloy.*

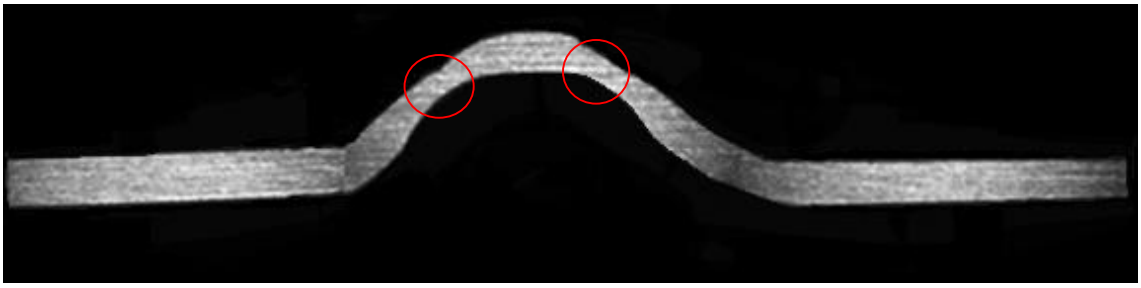

*Fig. 66. View of cross section of the specimen ECAP 110º after small punch testing with punch speed of 5 mm/min.*

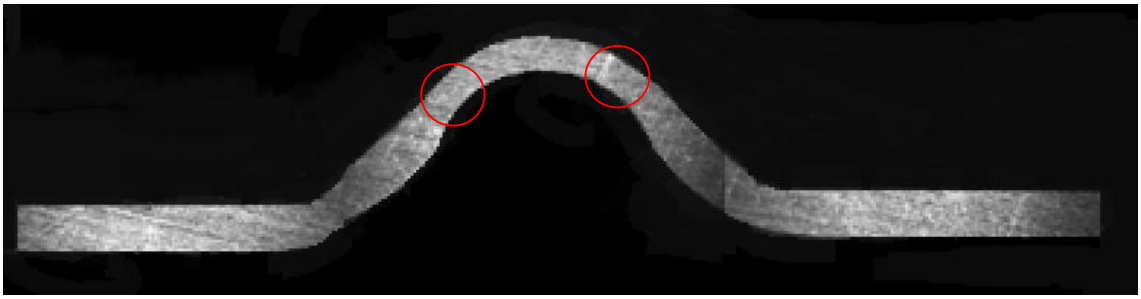

*Fig. 67. View of cross section of the specimen CG after small punch testing with punch speed of 5 mm/min.*

### 4.3.1. Calculations

Strain rate calculations based in the Jump test of each material. There are three for each at different points.

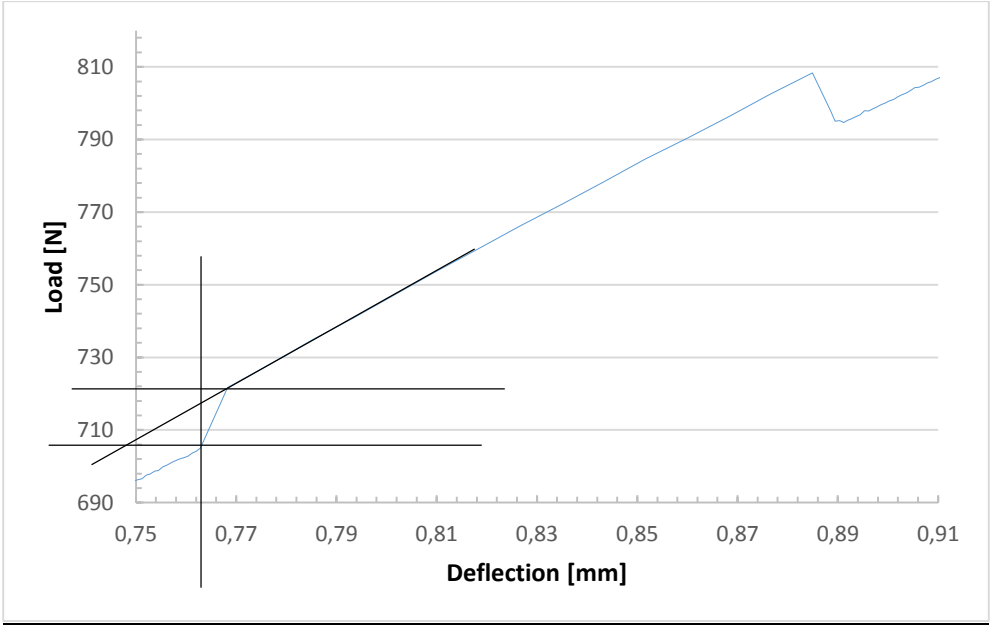


*Fig. 68. Fragment of load-central deflection curve from small punch testing of the CG alloy used for estimation of strain rate sensitivity.*

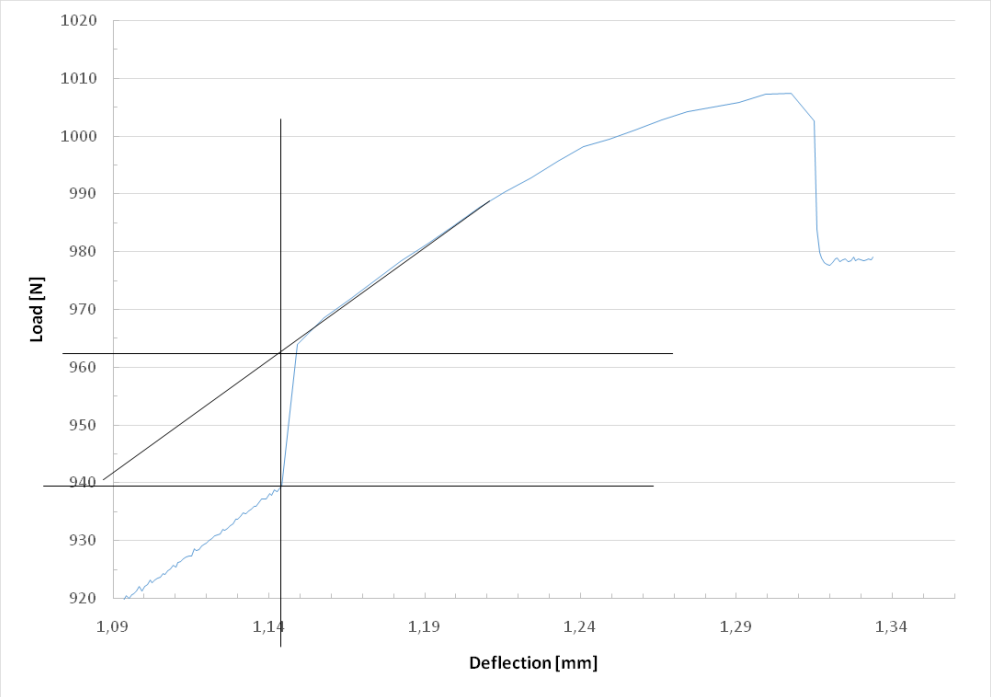


*Fig. 69. Fragment of load-central deflection curve from small punch testing of the CG alloy used for estimation of strain rate sensitivity.*

Table 5. Results of strain rate calculations for small punch testing.

| Material | SR1 | SR2 | SR3 |
|---|---|---|---|
| CG | 0.007 | 0.003 | 0.007 |
| ECAP110 | 0.013 | 0.010 | 0.010 |
| ECAP90 | 0.012 | 0.016 | 0.014 |

Table 6. Results of estimation of true strain induced by biaxial stretching into small punch specimens.

| Material | CG | | | ECAP 110° | | | ECAP 90° | | |
|---|---|---|---|---|---|---|---|---|---|
| Speed [mm/min] | 0.05 | 0.5 | 5 | 0.05 | 0.5 | 5 | 0.05 | 0.5 | 5 |
| $\dot{\varepsilon}$ | 0.39 | 0.49 | 0.39 | 0.37 | 0.31 | 0.53 | 0.40 | 0.38 | 0.48 |

# 5 CONCLUSIONS

# 5. Conclusions

Following conclusions can be made based on the results of this investigation.

1) There is a strong effect of ECAP processing route on the microstructure of the Cu-0.6Cr-0.08Zr alloy. ECAP processing using a die with an angle of 110$^{o}$ with total strain of 6.5 results in formation of very inhomogeneous microstructure consisting of cells, ultra-fine subgrains, low fraction of ultra-fine grains and containing high dislocation density. An increase of ECAP strain from 6.5 to 9.2 via using die having an angle of 90$^{o}$ diminishes cell and results in increase of fraction of high angle grain boundaries and in higher fraction of ultra-fine grains having lower size.

2) Mechanical strength (yield strength and ultimate tensile strength) of the Cu-0.6Cr-0.08Zr alloy dramatically increases after ECAP processing, whereas its uni-axial tensile ductility (uniform elongation and elongation to failure) significantly decreases. There is a strong effect of SPD microstructure on mechanical behavior of the material. Finer grains and higher fraction of high angle grain boundaries in the material processed with higher ECAP strain (9.2) result in higher mechanical strength and somewhat higher ductility, compared to the material after ECAP processing with lower strain (6.5).

3) Grain refinement down to ultra-fine scale also enhances strain rate sensitivity of the of the Cu-0.6Cr-0.08Zr alloy by a factor of 3. It should be noted that there is an effect of deformation mode (uni-axial tensile test and biaxial stretching) on the strain rate sensitivity. The material in all conditions shows lower strain rate sensitivity during small punch testing. This can be related to both change of deformation mode, which in turn affects the dislocation-related deformation mechanisms, and possible effect of friction.

4) Despite ECAP processed Cu-0.6Cr-0.08Zr alloy has very low uni-axial tensile ductility, it shows high biaxial stretching formability, comparable to that of its coarse-grain counterpart and sufficient for metalforming operations. Biaxial stretching formability of the ECAP processed alloy tends to increase with increasing punch speed to 5 mm/min due to enhanced ability of the material to accumulate dislocations while tested at high strain rates.

# 6 REFERENCES

# 6. References

[1] T.G. Langdon. Acta Mater. 61 (2013) 7035.

[2] R.Z. Valiev, O. A. Kaibyshev, R.I. Kuznetsov, R.Sh. Musalimov, N.K. Tsenev. Dokl. Akad. Nauk SSSR. 301 (1988) 864.

[3] R.Z. Valiev, A.P. Zhilyaev, T.G. Langdon. John Wiley & Sons, Hoboken, New Jersey, USA, (2014) 456.

[4] V.M. Segal. Mater. Sci. Eng. A197 (1995) 157.

[5] V.M. Segal. Mater. Sci. Eng. A271 (1999) 322.

[6] M. Furukawa, Z. Horita, M. Nemoto, T.G. Langdon. J. Mater. Sci. 36 (2001) 2835.

[7] V.M. Segal. Mater. Sci. Eng. A338 (2002) 331.

[8] V.M. Segal. Mater. Sci. Eng. A345 (2003) 36.

[9] V.M. Segal. Mater. Sci. Eng. A386 (2004) 269.

[10] Y. Iwahashi, J. Wang, Z. Horita, M. Nemoto, T.G. Langdon. Scripta Mater. 35 (1996) 143.

[11] F.Z. Utyashev, F.U. Enikeev, V.V. Latysh. Ann. Chim. 21 (1996) 379.

[12] D.N. Lee. Scripta Mater. 43 (2000) 115.

[13] K. Xia, J. Wang. Metall. Mater. Trans. 32A (2000) 2639.

[14] T. Aida, K. Matsuki, Z. Horita, T.G. Langdon. Scripta Mater. 44 (2001) 575.

[15] Y. Wu, I. Baker. Scripta Mater. 37 (1997) 437.

[16] A. Shan, I.G. Moon, H.S. Ko, J.W. Park. Scripta Mater. 41 (1999) 353.

[17] Y. Iwahashi, Z. Horita, M. Nemoto, T.G. Langdon. Acta Mater. 45 (1997) 4733.

[18] K. Furuno, H. Akamatsu, K. Oh-ishi, M. Furukawa, Z. Horita, T.G. Langdon. Acta Mater. 52 (2004) 2497.

[19] M. Nemoto, Z. Horita, M. Furukawa, T.G. Langdon. Metals Mater. 4 (1998) 1181.

[20] Z. Horita, M. Furukawa, M. Nemoto, T.G. Langdon. Mater. Sci. Tech. 16 (2000) 1239.

[21] M. Furukawa, Z. Horita, T.G. Langdon. Metals Mater. 9 (2003) 141.

[22] K. Nakashima, Z. Horita, M. Nemoto, T.G. Langdon. Mater. Sci. Eng. A281 (2000) 82.

[23] S. Lee, T.G. Langdon. Mater. Res. Soc. Symp. Proc. 601 (2000) 359.

[24] K. Valdés León, M.A. Muñoz-Morris, D.G. Morris. Mater. Sci. Eng. 536 (2012) 181.

[25] R. Pippan, S. Scheriau, A. Taylor, M. Hafok, A. Hohenwarter, A. Bachmaier. Ann. Rev. Mater. Res. 40 (2010) 319.

[26] K. Kitagawa, K. Kita, M. Gotoh, N. Takata, N. Tsuji. Mater. Sci. 584-586 (2008) 791.

[27] Y. Estrin, A. Vinogradov. Acta Mater. 61 (2013) 782.

[28] E.O. Hall. Proc. Phys. Soc. B 64 (1951) 747.

[29] N.J. Petch. J. Iron Steel Inst. 174 (1953) 25.

[30] R.Z. Valiev, N.A. Enikeev, M.Yu. Murashkin, V.U. Kazykhanov, X. Sauvage. Scr. Mater. 63 (2010) 949.

[31] H.J. Choi, S.W. Lee, J.S. Park, D.H. Bae. Scr. Mater. 59 (2008) 1123.

[32] A. Loucif, R.B. Figueiredo, T. Baudin, F. Brisset, R. Chemam, T.G. Langdon. Mater. Sci. Eng. A 532 (2012) 139.

[33] Z. Horita, T. Fujinami, M. Nemoto, T.G. Langdon. Metall. Mater. Trans. 31A (2000) 691.

[34] Y.T. Zhu, T.G. Langdon. JOM 56(10) (2004) 58.

[35] I. Sabirov, M.Yu. Murashkin, R.Z. Valiev. Mater. Sci. Eng. A 560 (2013) 1.

[36] Y. Zhao, Y.T. Zhu, E.J. Lavernia. Adv. Eng. Mater. 12 (2010) 76.

[37] E. Ma. JOM 58 (4) (2006) 49.

[38] G.E. Dieter. Mechanical Metallurgy, McGraw-Hill, Boston, 1986.

[39] E.W. Hart. Acta Metal. Mater. 15 (1967) 351.

[40] R.Z. Valiev, I.V. Alexandrov, T.C. Lowe, Y.T. Zhu. J. Mater. Res. 17 (2002) 5.

[41] H.T. Zhou, J.W. Zhong, X. Zhou, Z.K. Zhao, Q.B. Li. Mater. Sci. Eng. A 498 (2008) 225.

[42] V.R. Barabash, G.M. Kalinin, S.A. Fabritsiev, S.J. Zinkle. Nucl. Mater. 417 (2011) 904.

[43] P. Lorenzetto, A. Peacock, I. Bobin-Vastra, L. Briottet, P. Bucci, G. Dell'Orco, K. Ioki, M. Roedig, P. Sherlock. Fusion Eng. Des. 81 (2006) 355.

[44] T.G. Langdon. Mater. Sci. Eng. A 462 (2007) 3.

[45] A.P. Zhilyaev, T.G. Langdon. Prog. Mater. Sci. 53 (2008) 893.

[46] K.J. Kurzydłowski. Mater. Sci. Forum 503-504 (2006)341.

[47] W.X. Qi, J.P. Tu, F. Liu, Y.Z. Yang, N.Y. Wang, H.M. Lu, X.B. Zhang, S.Y. Guo, M. S. Liu. Mater. Sci. Eng. A343 (2003) 89.

[48] J.P. Tu, L. Meng, M.S. Liu. Wear 220 (1998) 72.

[49] S. Kang. Wear162–164 (1993) 1123.

[50] I. Sağlam, D. Özyürek, K. Çetinkaya. Bull. Mater. Sci. 34 (2011) 1465.

[51] K.D. Ralston, N. Birbilis. Corrosion 66 (2010) 075005.

[52] K.D. Ralston, N. Birbilis, C.H.J. Davies. Scr. Mater. 63 (2010) 1201.

[53] K.D. Ralston, D. Fabijanic, N. Birbilis. Electrochim. Acta 56 (2011) 1729.

[54] W. Wei, K.X. Wei, Q.B. Du. Mater. Sci. Eng. A 454–455 (2007) 536.

[55] M.M. Sharma, C.W. Ziemian. J. Mater. Eng. Perform. 17 (2008) 870.

[56] M.F. Naeini, M.H. Shariat. M. Eizadjou. J. Alloys Compd. 509 (2011) 4696.

[57] M. Hockauf, L.W. Meyer, D. Nickel, G. Alisch, T. Lampke, B. Wielage, L. Krueger. J. Mater. Sci. 43 (2008) 7409.

[58] E. Sikora, X.J. Wei, B.A. Shaw. Corrosion 60 (2004) 387.

[59] K.D. Ralston, N. Birbilis, M.K. Cavanaugh, M. Weyland, B.C. Muddle, R.K.W. Marceau. Electrochim. Acta 55 (2010) 7834.

[60] J.G. Brunner, J. May, H.W. Hoeppel, M. Goeken, S. Virtanen. Electrochim. Acta 55 (2010) 1966.

[61] K.D. Ralston, J.G. Brunner, S. Virtanen, N. Birbilis. Corrosion 67 (2011) 105001.

[62] M.K. Chung, Y.S. Choi, J.G. Kim, Y.M. Kim, J.C. Lee. Mater. Sci. Eng. A 366 (2004) 282.

[63] T.S. Mahmoud. J. Mech. Eng. Sci. 222 (2008) 1117.

[64] W. Wei, K.X. Wei, Q.B. Du, Mater. Sci. Eng. A 454–455 (2007) 536.

[65] M.M. Sharma, C.W. Ziemian. J. Mater. Eng. Perform. 17 (2008) 870.

[66] M.F. Naeini, M.H. Shariat, M. Eizadjou. J. Alloys Compd. 509 (2011) 4696.

[67] M. Hockauf, L.W. Meyer, D. Nickel, G. Alisch, T. Lampke, B. Wielage, L. Krueger. J. Mater. Sci. 43 (2008) 7409.

[68] M.M. Sharma, C.W. Ziemian. J. Mater. Eng. Perform. 17 (2008) 870.

[69] A. Vinogradov, V. Patlan, Y. Suzuki, K. Kitagawa, V.I. Kopylov. Acta Mater. 50 (2002) 1639.

[70] R. Egerton, Physical principles of electron microscopy. Springer US, New York City (2005) 11.

[71] H.H. Rose. Sci. Tech. Adv. Mater. 9 (2008) 014107.

[72] D. Stojakovic. P.A.C. 6 (2012) 1.

[73] V. Randle. Mater. Charact. 60 (2009) 913.

[74] A. Jiang, W. Godfrey, Q. Liu. Mater. Sci. Eng. A 483-84 (2008) 576.

[75] D. Raabe, A. Bastos, S. Zaefferer, C. Schuh. Acta Mater. 54 (2006) 2451.

[76] V. Randle, G.S. Rohrer, H.M. Miller, M. Coleman, G.T. Owen. Acta Mater. 56 (2008) 2363.

[77] M.G. Perez, E.A. Kenik, M.J. O'Keefe, F.S. Miller, B. Johnson. Mater. Sci. Eng. A, 424 (2006) 239.

[78] A.J. Wilkinson, G. Meaden, D.J. Dingley. Ultramicroscopy 106 (2006) 307.

[79] M.K. Adam, J. Schwartz, B.L. Adams, D.P. Field. Electron Backscatter Diffraction in Materials Science. Springer US, New York City, 2009.

[80] G. E. Dieter. Mechanical metallurgy. McGraw-Hill, New York 1976.

[81] J. R. Davis. Tensile Testing, 2nd Edition: ASM International, 2004.

[82] D. Caillard, J.L. Martin. Thermally Activated Mechanisms in Crystal Plasticity, Pergamon Materials Series, Vol. 8, Elsevier. Oxford, 2003.

[83] D.T Blagoeva, R. C. Hurst. Mater. Sci. Eng. A 510–511 (2009) 219.

[84] J. Autillo, M. A. Contreras, C. Betegón, C. Rodríguez, F.J. Belzunce. Utilización del ensayo miniatura de punzonamiento (small punch test) en la caracterización mecánica de aceros, Escuela Politécnica Superior de Ingeniería de Gijón, Universidad de Oviedo. Anales de Mecánica de la Fractura Vol. I (2006) 77.

[85] Z. Wang, H. Shi, J. Lu, P. Shi, X. Ma. Nucl. Eng. Des. 238 (2008) 3186.

[86] R. Kapoor, N. Kumar, R.S. Mishra, C.S. Huskamp, K.K. Sankaran, Mater. Sci. Eng. A 527 (2010) 5246.

[87] A. Kelly, R.B. Nicholson. Strengthening methods in crystals. Elsevier, Essex, UK, 1971.

[88] Y.W. Ma, K.B. Yoon. Mater. Sci. Eng. A Vol. 527 (2010) 3630.

[89] E. Fleury, J.S. Ha. Int. J. Press. Vessel. Pip. vol. 75 (1998) 699.